

Scalable quantum error mitigation with phase-cycled dynamical decoupling

Weibin Ni^{1,2}, Zhijie Li³, Guanyu Qu³, Zhecheng Sun^{2,4}, Jiale Dai^{1,2}, Fazhan Shi^{3,5}, and Lei Sun^{1,2,4,*}

¹Department of Physics, School of Science and Research Center for Industries of the Future, Westlake University, Hangzhou 310030, Zhejiang Province, China

²Institute of Natural Sciences, Westlake Institute for Advanced Study, Hangzhou 310024, Zhejiang Province, China

³Laboratory of Spin Magnetic Resonance, School of Physical Sciences, Anhui Province Key Laboratory of Scientific Instrument Development and Application, University of Science and Technology of China, Hefei 230026, China

⁴Department of Chemistry, School of Science and Research Center for Industries of the Future, Westlake University, Hangzhou 310030, Zhejiang Province, China

⁵School of Biomedical Engineering and Suzhou Institute for Advanced Research, University of Science and Technology of China, Suzhou 215123, China

*E-mail: sunlei@westlake.edu.cn

1 Abstract

The realization of quantum technologies in the Noisy Intermediate-Scale Quantum era is severely constrained by qubit decoherence and control errors, presenting fundamental challenges to achieving quantum advantages. Dynamical decoupling is a widely used, powerful technique for decoherence error suppression. However, it is susceptible to control errors, making non-robust sequences like UDD impractical to implement and robust ones like CPMG to significantly overestimate decoherence times. This overestimation issue remains largely unexplored in the past few decades, leading to many reports of exceptionally long yet plausible decoherence times across various qubit platforms. Here, we construct Hadamard phase cycling as a non-Markovian quantum error mitigation method for dynamical decoupling. This method exploits group structure to design phase configurations of equivalent ensemble quantum circuits, effectively eliminates circuit outputs generated from erroneous dynamics, and scales linearly with circuit depth. Harnessing its error mitigation capability for ensemble solid-state electron spin qubits embedded in paramagnetic molecules and nitrogen-vacancy centers in diamond enables accurate acquisition of decoherence times. Applying Hadamard phase cycling on single trapped ion and superconducting transmon qubits effectively preserves their state fidelity during dynamical decoupling. The integration of scalable quantum error mitigation and suppression would facilitate the development of quantum technologies with noisy qubits and control hardware.

2 Introduction

Quantum information science holds great promise for delivering transformative computational power, metrological sensitivity, and communication security beyond classical limits[1]. In the current Noisy Intermediate-Scale Quantum (NISQ) era, the realization of quantum advantages is hampered by susceptibility of qubits to decoherence and control errors[2]. In principle, quantum error correction can eliminate these errors and enable fault-tolerant quantum technologies, but it imposes stringent demands on error rates and requires a substantial overhead of physical qubits—conditions that are presently beyond technological reach[3, 4].

Dynamical decoupling, which applies a pulse sequence to average out unwanted environment–system coupling, is widely applied to suppress the decoherence error[5–7]. Remarkably, it could significantly extend decoherence times (T_2) for versatile qubit platforms, e.g. nuclear spins[8], solid-state spin defects[9–12], neutral atoms[13], superconducting circuits[14, 15], trapped ions[16], semiconductor quantum dots[17, 18], paramagnetic molecules[19–21], etc. The capability of coherence preservation enables applications of dynamical decoupling across a wide range of quantum technologies, including Hamiltonian engineering in quantum simulation[22], noise spectrum reconstruction[23, 24], sensitive and selective quantum

metrology[25], and state protection in quantum computing[26]. However, dynamical decoupling itself is prone to control errors, causing accumulation of erroneous dynamic evolution of quantum states that leads to low state fidelity. Although some dynamical decoupling sequences, e.g. CPMG, XY-8, and XY-16, are designed with inherent robustness to protect the fidelity of final state[27], control errors may still reduce the fidelity of intermediate states and compromise characterization of dynamic properties[28]. Therefore, albeit extensively used for acquiring T_2 , these robust sequences tend to significantly overestimate T_2 under control errors. This problem, which remains not fully addressed over several decades, would misguide the design and optimization of qubits[29].

To this end, quantum error mitigation (QEM) has emerged as a highly feasible strategy to handle control errors of pulses (i.e. single quantum gates)[30]. By post-processing outputs from an ensemble of noisy quantum circuits, QEM reduces the impact of errors and more accurately estimates expectation values of observables. Techniques like zero-noise extrapolation[4, 31, 32], probabilistic error cancellation[33, 34], and symmetry constraints[35, 36] have established QEM as a viable tool for current quantum hardware, with applications spanning variational quantum eigensolvers[37], entanglement entropy measurements[38], and logical error mitigation[39]. Nonetheless, existing approaches have paid little attention to composition analysis of noisy outputs or design of equivalent circuits, which could provide theoretical guidance for mitigating control errors in specific tasks like dynamical decoupling.

Interestingly, an alternative error mitigation method, phase cycling, has been developed decades ago in the context of nuclear magnetic resonance and then extended to electron paramagnetic resonance[40], magnetic resonance imaging[41], optical spectroscopy[42], etc. Typically, phase cycling employs a set of functionally equivalent quantum circuits (or pulse sequences) leveraging their phase degree of freedom. The phase configurations are systematically designed by classifying qubit dynamics based on their evolution pathways[43]. This approach selectively extracts the desired dynamics (i.e. error-free channels) by averaging observables obtained from all circuits. Hence, phase cycling is a novel non-Markovian QEM yet both its potential in quantum information science and its application for dynamical decoupling have remained largely unexplored.

Here, we show that for systems whose relaxation time (T_1) well exceeds T_2 and where single gate fidelity is relatively low, dynamical decoupling without proper mitigation of control errors tends to severely overestimate T_2 or become impractical to implement. Complete error mitigation demands exponential scaling with the circuit depth according to the selection rule of coherence-only dynamic processes, yet it can be well approximated with linear scaling by quantum circuits whose phase configurations forming an abelian group. Based on this property, we design Hadamard phase cycling, the first practical QEM method for inversion-pulse-based dynamical decoupling (IDD) including CP, CPMG, XY-8, XY-16, and UDD that are widely used in quantum information science and magnetic resonance. Applying this protocol to IDD enables accurate measurement and significant enhancement of T_2 for

ensemble electron spin qubits embedded in paramagnetic molecules and nitrogen-vacancy (NV) centers in diamond. Benchmarking it on single trapped $^{40}\text{Ca}^+$ ion and superconducting transmon qubits yields near-quantitative effective state fidelity.

3 Results

3.1 Practical phase cycling for IDD

We consider a qubit whose resonant frequency dominates the Hamiltonian. Under this assumption, the state of qubit can be described by a linear combination of coherence orders $p = \pm 1, 0$ corresponding to $S_{\pm} = S_x \pm iS_y$ and S_z , respectively, where $S_{x,y,z}$ are Pauli matrices. Here, $p = \pm 1$ ($p = 0$) represents coherence (population) and the corresponding state undergoes decoherence (relaxation) process with a characteristic time T_2 (T_1). A pulse could transform a coherence order into up to three with various weights. A long pulse sequence generates an exponential number of coherence transfer pathways, each of which reflects a specific dynamic process. Certain dynamic processes can be selected via phase cycling.

Most previous studies conducted IDD without phase cycling or with two-step phase cycling (TPC). TPC suffices to select desired dynamic processes only when all pulses are error-free, whereas noisy inversion pulses induce unintended coherence-order changes ($\Delta p = \pm 1$) and cause coherence-population mixing. The pathways consisting of only $p = \pm 1$ states generate desired echoes reflecting pure decoherence; those involving $p = 0$ states generate undesired echoes that undergo intermittent relaxation processes (Fig. 1a). To illustrate this point, we applied a modified CPMG sequence on an ensemble of Cu^{2+} -based molecular qubits to separate desired and undesired echoes (Fig. 1c)[44]. The former decays more than 600 times faster than the latter (Fig. 1e). In standard CPMG experiments (Fig. 1b), these two types of echoes overlap, causing TPC to overestimate T_2 that leads to positively biased thereby misleading assessment of qubit performance.

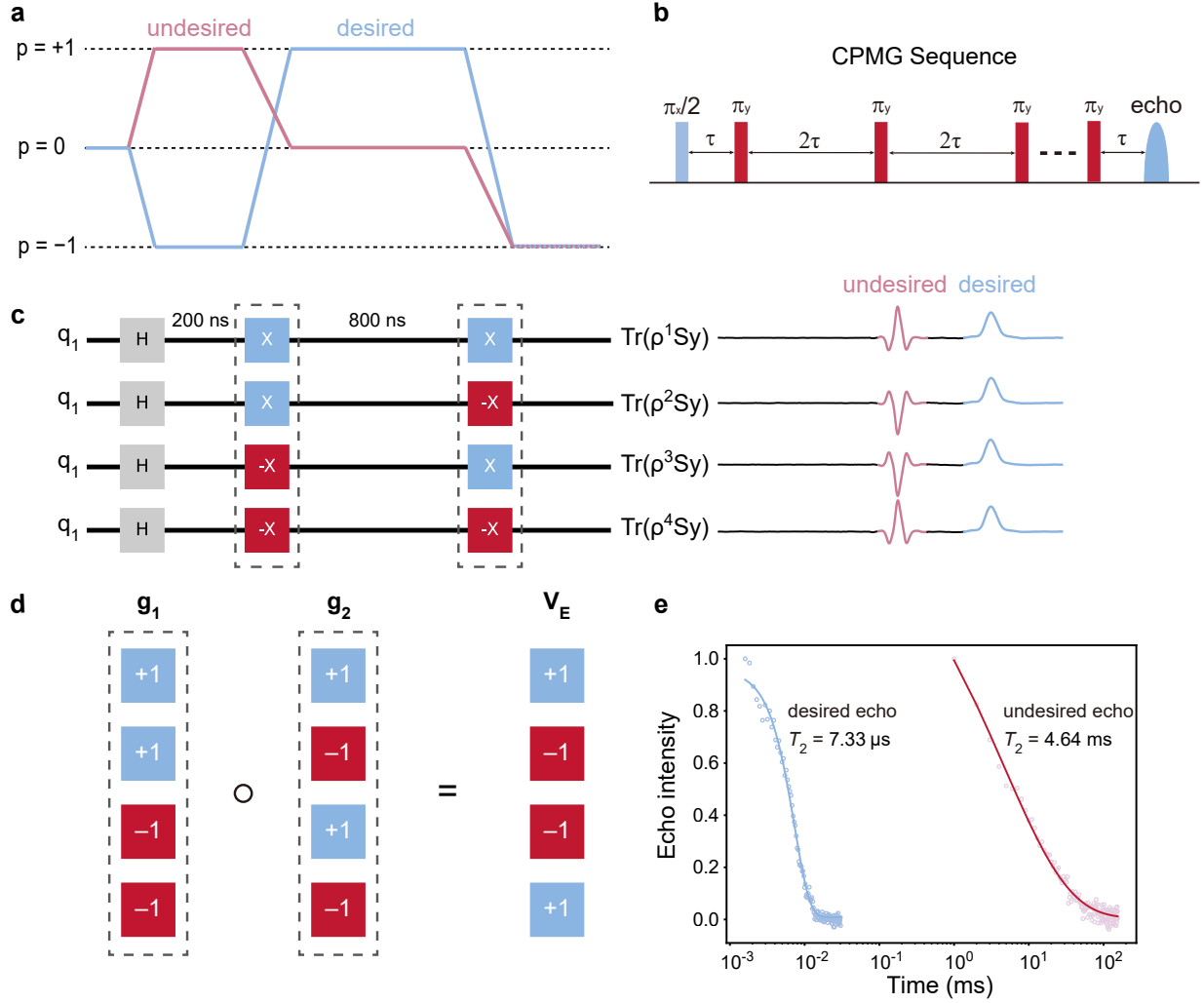


Fig. 1. Introduction to phase cycling. **a**, Desired and undesired coherence transfer pathways. **b**, Composition of CPMG sequence. It includes a $\pi/2$, coherence-generation pulse and a train of spin-locking inversion pulses. **c**, CPC for modified CPMG-2. q_1 and H represent qubit and Hadamard gate, respectively. $\pm X$ represent inversion pulses with opposite phases. $Tr(\rho^i S_y)$ represents the expectation value of S_y in the final state ρ^i of the i^{th} quantum circuit. Schemes on right are experimental outputs of quantum circuits with desired and undesired echoes highlighted. **d**, Example of Hadamard product orthogonality for the undesired echo in **c**. **e**, Echo decay curves of desired and undesired echoes. Data were collected for ensemble Cu^{2+} -based molecular qubits at 8 K by varying the interval between two inversion pulses. The desired and undesired echoes decay with apparent T_2 of 7.33 μs and 4.64 ms, respectively.

Proper QEM of IDD requires selection of coherence-only dynamic processes. Consider an IDD- m sequence with m inversion pulses. The phase cycling includes d_m quantum circuits differing only in phase, and phase configurations of all pulses construct a set $G = \{g_1, \dots, g_m\}$ where g_i is a d_m -dimensional vector encompassing phases of the i^{th} inversion pulse. Naturally, coherence transfer pathways and corresponding echoes can be classified by indices of pulses causing coherence-population mixing (i.e. $\Delta p = \pm 1$) as they indicate where control errors need to be mitigated. For each class of pathways, we represent such indices by a set $F = \{f_1, \dots, f_k\}$, and define a d_m -dimensional vector V_E that encompasses phase shifts of echoes of all quantum circuits. As applying a π phase shift to any erroneous pulse flips all corresponding echoes (Fig. 1c, d), we construct g_i and V_E with binary numbers where +1 and -1 represent original and π -shifted phases, respectively. This construction naturally leads to

$$V_E = g_{f_1} \circ \dots \circ g_{f_k} \quad (1)$$

where “ \circ ” represents element-wise product, i.e. Hadamard product. Clearly, elimination of undesired echoes requires the sum of elements in V_E to be 0, a property defined as Hadamard product orthogonality. However, there are $\sum_{j=0}^m C_m^j = 2^m$ possible classes of pathways since any pulse could cause $\Delta p = \pm 1$. We thus define the ratio of classes fulfilling the Hadamard product orthogonality as orthogonality ratio, which reflects the effectiveness of error mitigation. Noticing that for G reaching 100% orthogonality ratio, no Hadamard product of two or more distinct elements of G belongs to G , we theoretically prove 2^m as the minimum value of d_m (see Supplementary Information). Hence, complete phase cycling (CPC), which completely mitigate control errors for IDD, demands at least 2^m quantum circuits—CPC is unscalable[19, 29, 45].

Despite its exponential complexity, CPC can be well approximated by constructing G with unique algebraic structures. For simplicity, we consider IDD- m with m being a power of 2. Notice that under Hadamard product, the abelian group structure guarantees linear scaling and near-quantitative orthogonality ratio. Accordingly, we construct Hadamard matrices, i.e. square matrices whose elements are ± 1 , by Sylvester’s method[46] and construct G with its column vectors forming an abelian group. This unique mathematical structure enables using m quantum circuits to achieve a high orthogonality ratio, which is above 96% for $m \geq 32$ (see Supplementary Information). We further improve the orthogonality ratio by harnessing the parity of coherence transfer pathways and integrate the resulting structure with TPC to construct HPC (Supplementary Fig. 1):

$$HPC = \begin{pmatrix} + & +\vec{1}_m & +\vec{1}_m & +H' \\ + & +\vec{1}_m & +\vec{1}_m & -H' \\ - & -\vec{1}_m & +\vec{1}_m & +H' \\ - & -\vec{1}_m & +\vec{1}_m & -H' \end{pmatrix}. \quad (2)$$

where the sign column determines whether to add or to subtract the results, $\vec{1}_m$ is an all-

ones vector of size m , and H' represents the Sylvester’s Hadamard matrix excluding its first column. Overall, the complexity of HPC scales linearly with m : it involves only $4m$ quantum circuits. This is a dramatic boost compared to the 2^m complexity of CPC. Meanwhile, HPC achieves an orthogonality ratio above 98% for $m > 16$ (Supplementary Fig. 2), where CPC begins impractical. Thus, HPC is both scalable and effective (Fig. 2a).

3.2 Quantum error mitigation for ensemble qubits

The non-Markovian nature of HPC enables its application for accurate T_2 acquisition. As proof of concept, we implemented Hadamard, complete, and two-step phase cycling (Fig. 2a) for CPMG- m to acquire T_2 of the ensemble Cu^{2+} -based molecular qubit. We first fixed the delay time between adjacent pulses while increasing the number of pulses. Hadamard and complete phase cycling yielded nearly identical echo intensities for each sequence with $m = 2 - 16$ (Fig. 2b). This phenomenon reinforces the nearly quantitative orthogonality ratio of HPC and shows the advantage of its linear scalability: for $m = 16$, HPC exerts 64 quantum circuits while CPC demands 65536 circuits. In sharp contrast, TPC leads to a much slower echo decay with increasing m , giving rise to significantly stronger echoes (Fig. 2b). This indicates substantial coherence-population mixing—TPC on noisy quantum circuits does not probe pure decoherence and more reliable phase cycling are indispensable to mitigate control errors.

The distinction between two-step and Hadamard phase cycling becomes critical when measuring T_2 with fixed number of pulses and variable delay times. Both methods exhibit an increase of the apparent T_2 with increasing sequence length, yet they display drastically different scaling factors: $T_2 \propto m^{0.42}$ for TPC and $T_2 \propto m^{0.17}$ for HPC (Fig. 2c). CPMG with TPC requires 256 pulses to improve T_2 by more than 10 times, whereas HPC would enforce nearly 0.9 million pulses should its scaling law be applicable to longer sequences. From another perspective, TPC would overestimate T_2 by an order of magnitude for CPMG-8192. Experimentally, CPMG-128 with HPC improves T_2 to 24 μs , approximately four times of the value obtained from Hahn echo decay (Supplementary Fig. 3), demonstrating its utility for coherence protection. Another ensemble radical-based molecular qubit system[47] exhibits similar behaviors (Supplementary Fig. 4).

We observed similar phenomena in another representative ensemble electron spin qubit system, i.e. NV centers in diamond (Fig. 2d). For CPMG- m experiments with fixed delay time, the echo intensity decays much faster under HPC than TPC as m increases (Fig. 2d). For those with fixed sequence length and variable delay time, TPC gives rise to longer apparent T_2 than HPC for CPMG-32 and CPMG-64 (Supplementary Fig. 5). Remarkably, employing CPMG-1536 with TPC yields an apparent T_2 approaching $0.25T_1$, indicating that such a long sequence mixes decoherence with relaxation (Fig. 2e). Overall, these experiments confirm that although TPC generates seemingly more promising coherence enhancement, it

inevitably involves coherence-population mixing and causes significant overestimation of T_2 . HPC, which balances effectiveness and scalability for error mitigation, provides a practical solution for T_2 acquisition of ensemble qubit systems.

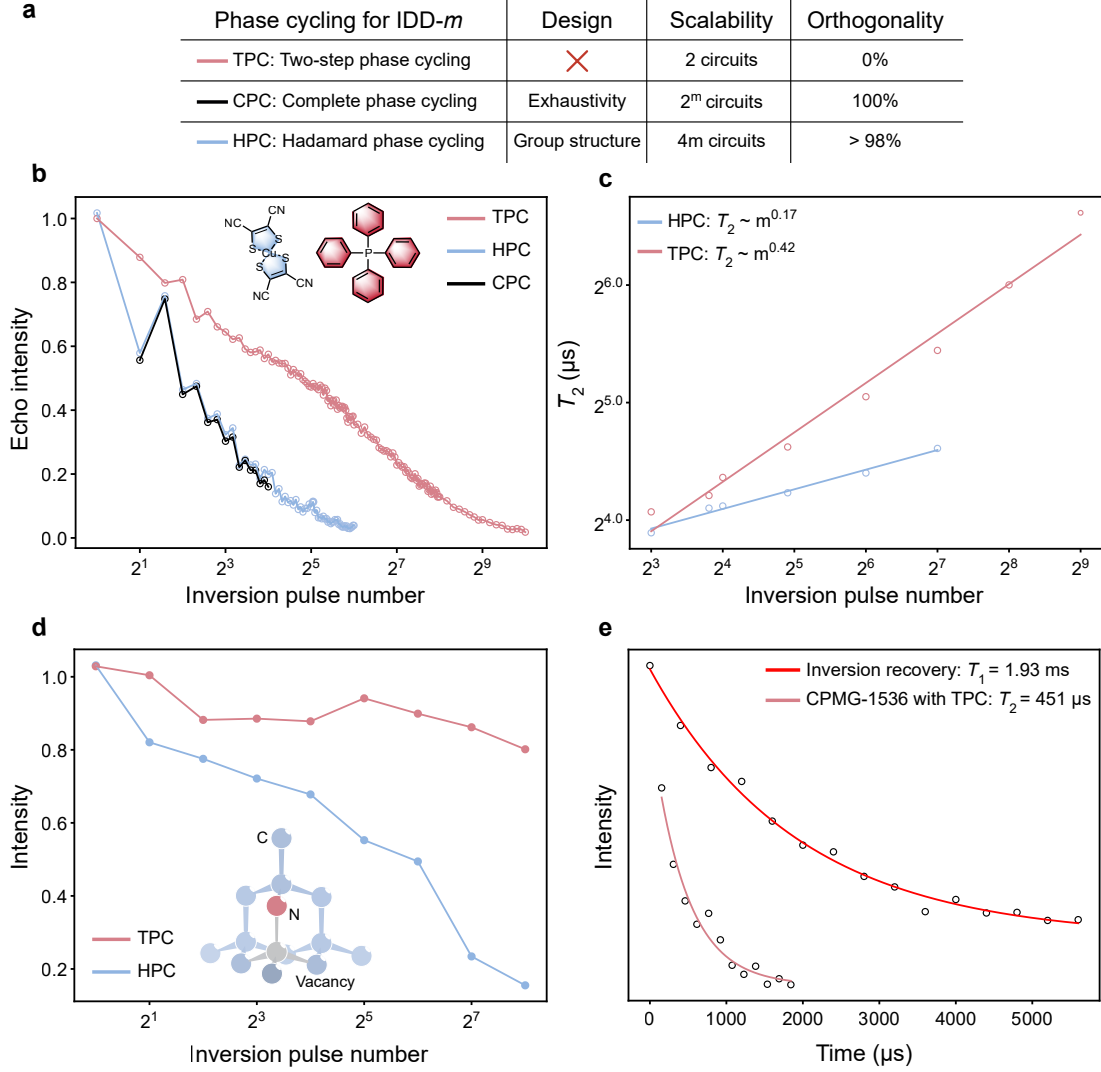


Fig. 2. T_2 measurements for ensemble electron spin qubits under CPMG. **a**, Introduction of different phase cycling methods. Assume that m is a power of 2 and $m > 16$ for which CPC becomes impractical. **b**, Comparison of echo intensities collected with HPC, CPC, and TPC. Inset: Schematic illustrations of the Cu^{2+} -based molecular qubit. **c**, Dependencies of T_2 on the number of inversion pulses for HPC and TPC. Data in **b** and **c** were collected on ensemble Cu^{2+} -based molecular qubits at 8 K. **d**, Comparison of echo intensities collected with HPC and TPC. Inset: Schematic illustrations of NV center in diamond. **e**, Inversion recovery curve and echo decay curve under CPMG-1536 with TPC. Data in **d** and **e** were collected on ensemble NV centers in diamond at room temperature. The x-axes of **b-d** and y-axis of **c** are in log scale.

HPC is also applicable to UDD, which is theoretically the optimal dynamical decoupling sequence under pure-dephasing model[48, 49] (Fig. 3a). For the Cu^{2+} -based molecular qubits, complete and Hadamard phase cycling again yielded well-defined echoes with identical intensities for UDD- m with $m = 2 - 10$ (Fig. 3b). In contrast, TPC generated complex echo signals with wrong phases likely due to overlapping of desired echoes with undesired ones (Fig. 3b inset). UDD- m with HPC shows $T_2 \propto m^{0.81}$ (Fig. 3c). The scaling factor is much larger than that of CPMG- m with HPC (0.17), demonstrating much better performance of UDD- m for decoherence error suppression. Specifically, UDD-8 slightly outperforms CPMG-64 (Fig. 3d), and UDD-14 improves T_2 to $35 \mu\text{s}$ that well exceeds the value observed for CPMG-128 ($T_2 = 24 \mu\text{s}$). Clearly, UDD is significantly undermined by control errors under TPC, which could prevent its correct implementation under noisy hardware and lead to misinterpretation and underestimation of its performance on decoherence error suppression. Thus, error mitigation, exemplified by HPC, is indispensable for reliable evaluation of dynamical decoupling sequences. The effectiveness of HPC on the robust, periodic CPMG and non-robust, aperiodic UDD proves that it is generally applicable to IDD. Such a universality provides HPC with extensive applications, ranging from rational design of dynamical decoupling sequences to quantum sensing and magnetic resonance imaging[25, 50].

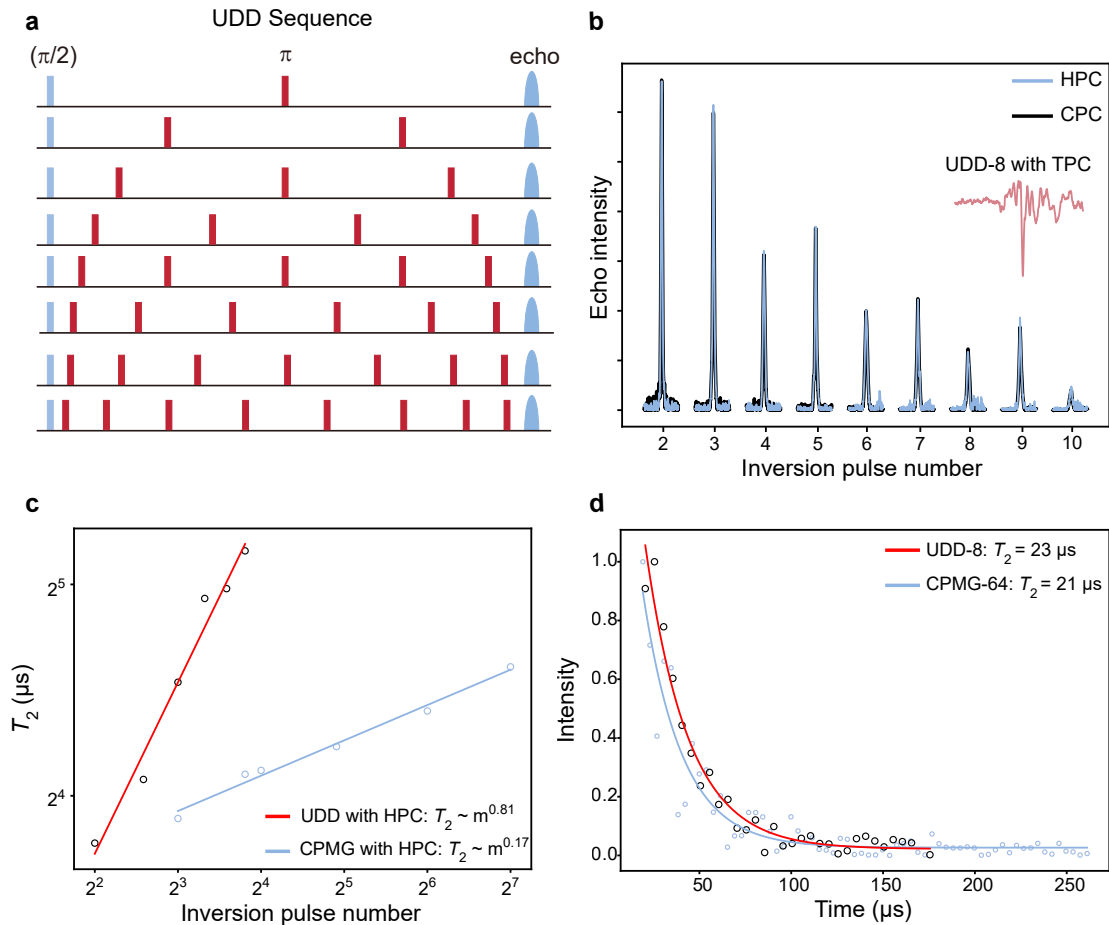


Fig. 3. Application of HPC for UDD on ensemble molecular qubits. **a**, Schematic illustrations of UDD-1 to UDD-8. **b**, Comparison of echo intensities collected with HPC and CPC. Inset: Echo signals observed for UDD-8 with TPC. **c**, Dependencies of T_2 on the number of inversion pulses for UDD and CPMG with HPC. Both axes are in log scale. **d**, Comparison of echo decay curves under UDD-8 and CPMG-64 with HPC. Data were collected on ensemble Cu^{2+} -based molecular qubits at 8 K.

3.3 Quantum error mitigation for single qubits

We further extend the application of phase cycling for single qubit platforms. Phase cycling averages out final quantum states of quantum circuits into a mixed state, which can be normalized into an effective pure state (ρ). Intuitively, this postprocessing, which is in line with the spirit of QEM, is equivalent to averaging multiple Bloch vectors into a unit vector that should coincide with the ideal state (σ). Hence, phase cycling can be benchmarked by effective state fidelity:

$$F^{eff} = (\text{Tr} \sqrt{\sqrt{\rho} \sigma \sqrt{\rho}})^2. \quad (3)$$

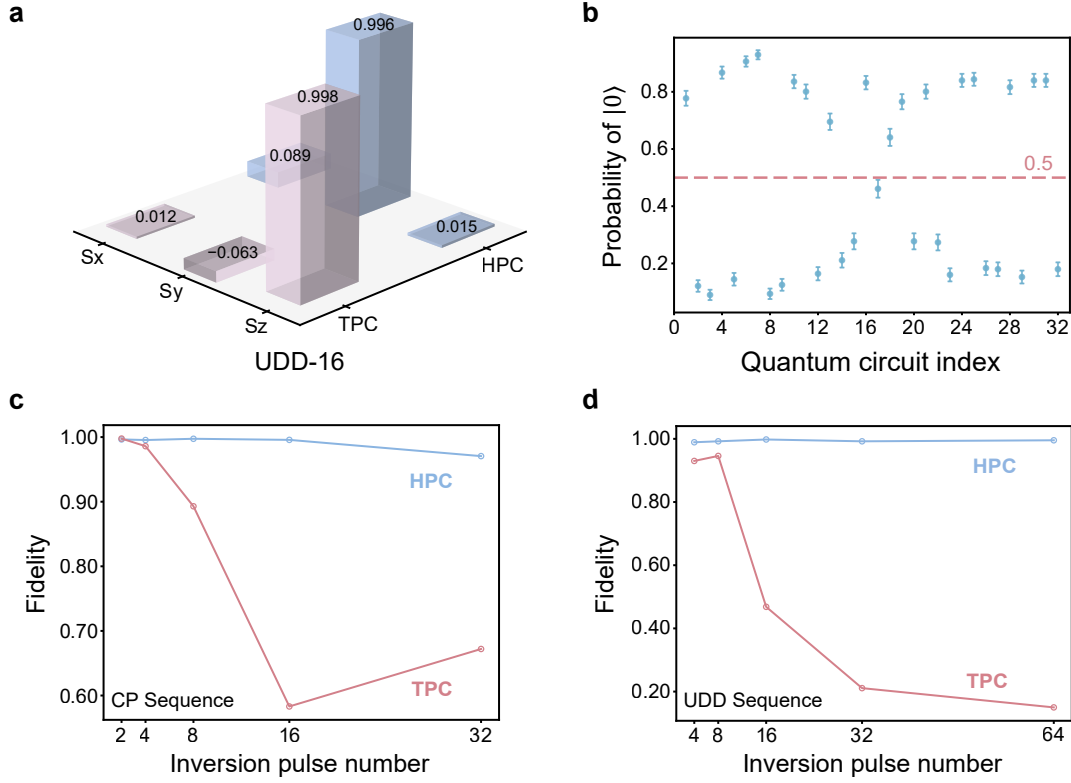


Fig. 4. HPC and effective state-fidelity tests on single trapped $^{40}\text{Ca}^+$ ion qubit. **a**, Quantum state tomography results of effective final states. **b**, Probability of being at $|0\rangle$ state for the final state of each quantum circuit. The average of all states is 0.508, indicating

nearly-zero z-component for the effective final state. **c,d**, Effective state fidelity under (c) CP and (d) UDD with HPC and TPC.

We experimentally benchmarked TPC and HPC on single trapped ion and superconducting qubits with CP- m and UDD- m sequences that lack inherent robustness. The final state of each quantum circuit was characterized by quantum state tomography. For CP- m with 2 – 16 inversion pulses exerted on single trapped $^{40}\text{Ca}^+$ ion qubit, HPC retains F^{eff} above 99.5% (Fig. 4c). In sharp contrast, the fidelity quickly declines to 58.3% for CP-16 with TPC. This trend was reproduced by UDD- m , where F^{eff} is 99.5% on UDD-64 with HPC yet it plummets to 15.0% with TPC (Fig. 4d). Single superconducting transmon qubit exhibits similar behaviors, with TPC significantly deteriorating the effective state fidelity while HPC maintains remarkable robustness under relatively large systematic error (Supplementary Fig. 6 and 7).

The key advantage of HPC lies in its ability to separate the qubit’s population and coherence, mimicking an ideal inversion pulse. It is evidenced by negligible z-component in the effective state (Fig. 4a), which is in stark contrast to the salient z-component observed in the final state of each individual quantum circuit (Fig. 4b; Supplementary Fig. 7). Therefore, given a relatively low single gate fidelity, dynamical decoupling itself is prone to erroneous dynamic evolution of intermittent states. HPC can mitigate the control error for every intermittent state, allowing reliable dynamical decoupling. As dynamical decoupling is routinely used to protect quantum information of idle qubits during quantum algorithms[3], its integration with scalable phase cycling could improve the performance of quantum computing.

4 Discussion

In conclusion, leveraging the phase degree of freedom in quantum circuits and the orthogonality of group structure, we designed Hadamard phase cycling as the first practical non-Markovian quantum error mitigation for inversion-pulse-based dynamical decoupling. This method balances effectiveness with scalability, enabling accurate measurement of T_2 and reliable implementation of dynamical decoupling with linear scaling for multiple leading qubit platforms. It would improve sensitivity and precision of NV-center-based nanoscale nuclear magnetic resonance, facilitate development of new dynamical decoupling towards quantum computing, and enhance the quality of T_2 -weighted magnetic resonance imaging. Our studies indicate that the utility of quantum error mitigation and suppression arises from a balance among complexity, effectiveness, and task-specific demands, rather than the pursuit of perfection. As these quantum error handling methods are likely compatible and mutually reinforcing, harnessing their synergy would open new avenues for NISQ-era quantum technologies.

5 Methods

5.1 Qubit platforms

Experiments on trapped ion qubits were conducted using a $^{40}\text{Ca}^+$ ion with Paul trap based on a CIQTEK ION I quantum processor, whose single gate fidelity was above 99.9%. Experiments on superconducting qubits were conducted using a transmon qubit of the Starmon-7 processor, accessed via the Quantum Inspire platform, whose single gate fidelity was well above 99%. X-band pulse electron paramagnetic resonance (EPR) spectroscopic characterization of molecular qubits was performed at 8K on a CIQTEK EPR100 spectrometer. The Cu^{2+} -based molecular qubit, $(\text{PPh}_4)_2[\text{Cu}(\text{mnt})_2]$ (PPh_4^+ = tetraphenylphosphonium; mnt^{2-} = 1,2-maleonitriledithiolate), was synthesized following literature procedure[44], and it was diluted in a diamagnetic isostructural host $(\text{PPh}_4)_2[\text{Ni}(\text{mnt})_2]$ with a concentration of 0.3%[20]. This molecule exhibits $T_1 = 37.03\text{ ms}$ and $T_2^{\text{Hahn}} = 6.54\text{ }\mu\text{s}$ revealed by inversion recovery and Hahn echo decay experiments, respectively (Supplementary Fig. 3). The radical-based molecular qubit, COF-5, was synthesized following literature procedure[47]. NV Centers used in this work have an average depth of 30 nm from the surface of diamond. Optical detected magnetic resonance experiments were performed with a homebuilt standard setup under an external magnetic field of approximately 315 G, with microwave phase errors less than 1 degree and frequency detuning less than 1.5 MHz. At room temperature, this sample exhibits $T_1 = 1.93\text{ ms}$ and $T_2^{\text{Hahn}} = 9.29\text{ }\mu\text{s}$ (Fig. 2e; Supplementary Fig. 5).

5.2 Dynamical decoupling sequences

CP sequences were implemented as $\pi_x/2 - [\tau - \pi_x - \tau]_n - \text{echo}$. CPMG sequences were implemented as $\pi_x/2 - [\tau - \pi_y - 2\tau - \pi_y - \tau]_n - \text{echo}$, where the phase of inversion pulse is shifted by π from the phase of the first $\pi/2$ pulse. The first inversion pulse's error within each block can be compensated by the following inversion pulse, giving rise to its inherent robustness. The implemented UDD- m involves m nonperiodic inversion pulses following a $\pi_x/2$ pulse, where all pulses have the same phase and the n^{th} inversion pulse is applied at[19, 49]:

$$t_n = t \sin^2 \frac{n\pi}{2(m+1)}, n = 1, \dots, m. \quad (4)$$

5.3 Two-step phase cycling

TPC involves two quantum circuits that differ only in phase of the first $\pi/2$ pulse; one uses a $\pi_x/2$ pulse and the other uses $\pi_{-x}/2$ pulse. Subtracting the results of these two circuits

effectively cancels baseline drift. For experiments on single trapped ion, superconducting qubits, and NV centers in diamond, an extra $\pi/2$ pulse is applied before measuring population distribution. In this case, phase cycling the final $\pi/2$ pulse also suffices.

5.4 Complete phase cycling

For IDD- m , the aforementioned CPC involves 2^m quantum circuits encompassing all possible phase configurations of inversion pulses[19, 29]. Practically, combination of CPC and TPC is required, where the phase of the first inversion pulse can be fixed so that the complexity does not change.

5.5 Hadamard phase cycling

Sylvester's method was used to construct Hadamard matrices[46]:

$$H_{2^n} = \begin{pmatrix} H_{2^{n-1}} & H_{2^{n-1}} \\ H_{2^{n-1}} & -H_{2^{n-1}} \end{pmatrix}, H_2 = \begin{pmatrix} 1 & 1 \\ 1 & -1 \end{pmatrix}. \quad (5)$$

where integer $n \geq 2$. For IDD- m , one needs to construct the smallest Sylvester's Hadamard matrix with dimension $2^n \geq m$ and drop the redundant columns. This property gives HPC's complexity between $4m$ and $8m - 8$. For simplicity, the orthogonality ratio of HPC was derived analytically for $m = 2^n$ by analyzing HPC's algebraic structure. All combinations of odd-numbered columns from H' satisfy Hadamard product orthogonality, and some combinations of even-numbered columns from H' do not satisfy. For an even number $2 \leq 2k < 2^n$, given $C_{2^n-1}^{2k}$ as the number of all possible combinations of choosing $2k$ columns from $2^n - 1$ columns in H' , the ratio of combinations that do not satisfy Hadamard product orthogonality is given by

$$p(2k) = \frac{1}{2^n} + (-1)^k \times \frac{2^n - 1}{2^n} \times \frac{C_{2^{(n-1)}-1}^k}{C_{2^n-1}^{2k}}. \quad (6)$$

5.6 Effective state fidelity

Define ρ^i as the final state of the i^{th} quantum circuit, and define phase-cycled expectation values as

$$v_{x,y,z} = \sum_i V_s^i Tr(\rho^i S_{x,y,z}), \quad (7)$$

where V_s^i is the i^{th} element of the sign vector; $Tr(\rho^i S_x)$ was obtained by adding a $\pi_{(-y)}/2$ pulse before measurement, and $Tr(\rho^i S_y)$ was obtained by adding a $\pi_x/2$ pulse. The normalized

$v_{x,y,z}$ were used to construct the effective state

$$\rho = \frac{1}{2}(S_0 + \langle v_x \rangle S_x + \langle v_y \rangle S_y + \langle v_z \rangle S_z). \quad (8)$$

where S_0 is two-dimensional identity matrix.

Data availability The data supporting our findings are included in the article and supplementary files. Additional data generated during the study are available from the corresponding author upon request.

References

- [1] David P DiVincenzo. Thirty years of quantum computing. *Quantum Science and Technology*, 10(3):030501, 2025.
- [2] John Preskill. Quantum computing in the NISQ era and beyond. *Quantum*, 2:79, 2018.
- [3] Google Quantum AI and Collaborators. Quantum error correction below the surface code threshold. *Nature*, 638(8052):920–926, 2025.
- [4] Youngseok Kim, Andrew Eddins, Sajant Anand, Ken Xuan Wei, Ewout van den Berg, Sami Rosenblatt, Hasan Nayfeh, Yantao Wu, Michael Zaletel, Kristan Temme, and Abhinav Kandala. Evidence for the utility of quantum computing before fault tolerance. *Nature*, 618(7965):500–505, 2023.
- [5] P. C. Maurer, G. Kucsko, C. Latta, L. Jiang, N. Y. Yao, S. D. Bennett, F. Pastawski, D. Hunger, N. Chisholm, M. Markham, D. J. Twitchen, J. I. Cirac, and M. D. Lukin. Room-temperature quantum bit memory exceeding one second. *Science*, 336(6086):1283–1286, 2012.
- [6] Hengyun Zhou, Joonhee Choi, Soonwon Choi, Renate Landig, Alexander M. Douglas, Junichi Isoya, Fedor Jelezko, Shinobu Onoda, Hitoshi Sumiya, Paola Cappellaro, Helena S. Knowles, Hongkun Park, and Mikhail D. Lukin. Quantum metrology with strongly interacting spin systems. *Physical Review X*, 10(3):031003, 2020.
- [7] Dieter Suter and Gonzalo A. Álvarez. Colloquium: Protecting quantum information against environmental noise. *Reviews of Modern Physics*, 88(4):041001, 2016.
- [8] S Meiboom and D Gill. Modified spin-echo method for measuring nuclear relaxation times. *Review of Scientific Instruments*, 29(8):688–691, 1958.
- [9] G. de Lange, Z. H. Wang, D. Ristè, V. V. Dobrovitski, and R. Hanson. Universal dynamical decoupling of a single solid-state spin from a spin bath. *Science*, 330(6000):60–63, 2010.

- [10] William K. Schenken, Simon A. Meynell, Francisco Machado, Bingtian Ye, Claire A. McLellan, Maxime Joos, V. V. Dobrovitski, Norman Y. Yao, and Ania C. Bleszynski Jayich. Long-lived coherences in strongly interacting spin ensembles. *Physical Review A*, 110(3):032612, 2024.
- [11] P. Siyushev, K. Xia, R. Reuter, M. Jamali, N. Zhao, N. Yang, C. Duan, N. Kukharchyk, A. D. Wieck, R. Kolesov, and J. Wrachtrup. Coherent properties of single rare-earth spin qubits. *Nature Communications*, 5(1):3895, 2014.
- [12] N. Bar-Gill, L.M. Pham, A. Jarmola, D. Budker, and R.L. Walsworth. Solid-state electronic spin coherence time approaching one second. *Nature Communications*, 4(1):1743, 2013.
- [13] Chang Hoong Chow, Boon Long Ng, and Christian Kurtsiefer. Coherence of a dynamically decoupled single neutral atom. *Journal of the Optical Society of America B*, 38(2):621, 2021.
- [14] Bibek Pokharel, Namit Anand, Benjamin Fortman, and Daniel A. Lidar. Demonstration of fidelity improvement using dynamical decoupling with superconducting qubits. *Physical Review Letters*, 121(22):220502, 2018.
- [15] Nic Ezzell, Bibek Pokharel, Lina Tewala, Gregory Quiroz, and Daniel A. Lidar. Dynamical decoupling for superconducting qubits: A performance survey. *Physical Review Applied*, 20(6):064027, 2023.
- [16] Pengfei Wang, Chun-Yang Luan, Mu Qiao, Mark Um, Junhua Zhang, Ye Wang, Xiao Yuan, Mile Gu, Jingning Zhang, and Kihwan Kim. Single ion qubit with estimated coherence time exceeding one hour. *Nature Communications*, 12(1):233, 2021.
- [17] M. Veldhorst, J. C. C. Hwang, C. H. Yang, A. W. Leenstra, B. de Ronde, J. P. Dehollain, J. T. Muhonen, F. E. Hudson, K. M. Itoh, A. Morello, and A. S. Dzurak. An addressable quantum dot qubit with fault-tolerant control-fidelity. *Nature Nanotechnology*, 9(12):981–985, 2014.
- [18] Elliot J. Connors, J. Nelson, Lisa F. Edge, and John M. Nichol. Charge-noise spectroscopy of Si/SiGe quantum dots via dynamically-decoupled exchange oscillations. *Nature Communications*, 13(1):940, 2022.
- [19] Jiangfeng Du, Xing Rong, Nan Zhao, Ya Wang, Jiahui Yang, and R. B. Liu. Preserving electron spin coherence in solids by optimal dynamical decoupling. *Nature*, 461(7268):1265–1268, 2009.
- [20] Yingqiu Dai, Yue Fu, Zhifu Shi, Xi Qin, Shiwei Mu, Yang Wu, Ji-Hu Su, Yi-Fei Deng, Lei Qin, Yuan-Qi Zhai, Yan-Zhen Zheng, Xing Rong, and Jiangfeng Du. Experimental protection of the spin coherence of a molecular qubit exceeding a millisecond. *Chinese Physics Letters*, 38(3):030303, 2021.

- [21] Jacob S. Feder, Benjamin S. Soloway, Shreya Verma, Zhi Z. Geng, Shihao Wang, Bethel B. Kifle, Emmeline G. Riendeau, Yeghishe Tsaturyan, Leah R. Weiss, Mouzhe Xie, Jun Huang, Aaron Esser-Kahn, Laura Gagliardi, David D. Awschalom, and Peter C. Maurer. A fluorescent-protein spin qubit. *Nature*, 645(8079):73–79, 2025.
- [22] W. Morong, K.S. Collins, A. De, E. Stavropoulos, T. You, and C. Monroe. Engineering dynamically decoupled quantum simulations with trapped ions. *PRX Quantum*, 4(1):010334, 2023.
- [23] Gonzalo A. Álvarez and Dieter Suter. Measuring the spectrum of colored noise by dynamical decoupling. *Physical Review Letters*, 107(23):230501, 2011.
- [24] Jonas Bylander, Simon Gustavsson, Fei Yan, Fumiki Yoshihara, Khalil Harrabi, George Fitch, David G. Cory, Yasunobu Nakamura, Jaw-Shen Tsai, and William D. Oliver. Noise spectroscopy through dynamical decoupling with a superconducting flux qubit. *Nature Physics*, 7(7):565–570, 2011.
- [25] Zhiyuan Zhao, Xiangyu Ye, Shaoyi Xu, Pei Yu, Zhiping Yang, Xi Kong, Ya Wang, Tianyu Xie, Fazhan Shi, and Jiangfeng Du. Sub-nanotesla sensitivity at the nanoscale with a single spin. *National Science Review*, 10(12):nwad100, 2023.
- [26] Hui Khoon Ng, Daniel A. Lidar, and John Preskill. Combining dynamical decoupling with fault-tolerant quantum computation. *Physical Review A*, 84(1):012305, 2011.
- [27] Alexandre M. Souza, Gonzalo A. Alvarez, and Dieter Suter. Robust dynamical decoupling. *Philosophical Transactions of the Royal Society A: Mathematical, Physical and Engineering Sciences*, 370(1976):4748–4769, 2012.
- [28] George Mitrikas and Rania Giourtsidou. Measuring reliable electron spin coherence times with dynamical decoupling sequences that use selective mw pulses. *Journal of Magnetic Resonance*, 381:107981, 2025.
- [29] Federico Lombardi, William K. Myers, Ji Ma, Junzhi Liu, Xinliang Feng, and Lapo Bogani. Dynamical nuclear decoupling of electron spins in molecular graphenoid radicals and biradicals. *Physical Review B*, 101(9):094406, 2020.
- [30] Zhenyu Cai, Ryan Babbush, Simon C. Benjamin, Suguru Endo, William J. Huggins, Ying Li, Jarrod R. McClean, and Thomas E. O’Brien. Quantum error mitigation. *Reviews of Modern Physics*, 95(4):045005, 2023.
- [31] Abhinav Kandala, Kristan Temme, Antonio D. Córcoles, Antonio Mezzacapo, Jerry M. Chow, and Jay M. Gambetta. Error mitigation extends the computational reach of a noisy quantum processor. *Nature*, 567(7749):491–495, 2019.
- [32] Ying Li and Simon C. Benjamin. Efficient variational quantum simulator incorporating active error minimization. *Physical Review X*, 7(2):021050, 2017.

- [33] Shuaining Zhang, Yao Lu, Kuan Zhang, Wentao Chen, Ying Li, Jing-Ning Zhang, and Kihwan Kim. Error-mitigated quantum gates exceeding physical fidelities in a trapped-ion system. *Nature Communications*, 11(1):587, 2020.
- [34] Kristan Temme, Sergey Bravyi, and Jay M. Gambetta. Error mitigation for short-depth quantum circuits. *Physical Review Letters*, 119(18):180509, 2017.
- [35] X. Bonet-Monroig, R. Sagastizabal, M. Singh, and T. E. O’Brien. Low-cost error mitigation by symmetry verification. *Physical Review A*, 98(6):062339, 2018.
- [36] Sam McArdle, Xiao Yuan, and Simon Benjamin. Error-mitigated digital quantum simulation. *Physical Review Letters*, 122(18):180501, 2019.
- [37] R. Sagastizabal, X. Bonet-Monroig, M. Singh, M. A. Rol, C. C. Bultink, X. Fu, C. H. Price, V. P. Ostroukh, N. Muthusubramanian, A. Bruno, M. Beekman, N. Haider, T. E. O’Brien, and L. DiCarlo. Experimental error mitigation via symmetry verification in a variational quantum eigensolver. *Physical Review A*, 100(1):010302, 2019.
- [38] Michael Foss-Feig, Stephen Ragole, Andrew Potter, Joan Dreiling, Caroline Figgatt, John Gaebler, Alex Hall, Steven Moses, Juan Pino, Ben Spaun, Brian Neyenhuis, and David Hayes. Entanglement from tensor networks on a trapped-ion quantum computer. *Physical Review Letters*, 128(15):150504, 2022.
- [39] Aosai Zhang, Haipeng Xie, Yu Gao, Jia-Nan Yang, Zehang Bao, Zitian Zhu, Jiachen Chen, Ning Wang, Chuanyu Zhang, Jiarun Zhong, Shibo Xu, Ke Wang, Yaozu Wu, Feitong Jin, Xuhao Zhu, Yiren Zou, Ziqi Tan, Zhengyi Cui, Fanhao Shen, Tingting Li, Yihang Han, Yiyang He, Gongyu Liu, Jiayuan Shen, Han Wang, Yanzhe Wang, Hang Dong, Jinfeng Deng, Hekang Li, Zhen Wang, Chao Song, Qiujiang Guo, Pengfei Zhang, Ying Li, and H Wang. Demonstrating quantum error mitigation on logical qubits. *arXiv:2501.09079*, 2025.
- [40] C Gemperle, G Aebli, A Schweiger, and R.R Ernst. Phase cycling in pulse EPR. *Journal of Magnetic Resonance*, 88(2):241–256, 1990.
- [41] Frank Ong, Joseph Y. Cheng, and Michael Lustig. General phase regularized reconstruction using phase cycling. *Magnetic Resonance in Medicine*, 80(1):112–125, 2018.
- [42] Suxia Yan and Howe-Siang Tan. Phase cycling schemes for two-dimensional optical spectroscopy with a pump–probe beam geometry. *Chemical Physics*, 360(1-3):110–115, 2009.
- [43] Geoffrey Bodenhausen, Herbert Kogler, and R.R. Ernst. Selection of coherence-transfer pathways in NMR pulse experiments. *Journal of Magnetic Resonance*, 213(2):276–294, 1983.

- [44] Katharina Bader, Dominik Dengler, Samuel Lenz, Burkhard Endeward, Shang-Da Jiang, Petr Neugebauer, and Joris van Slageren. Room temperature quantum coherence in a potential molecular qubit. *Nature Communications*, 5(1):5304, 2014.
- [45] Janne Soetbeer, Luis Fábregas Ibáñez, Zachariah Berkson, Yevhen Polyhach, and Gunnar Jeschke. Regularized dynamical decoupling noise spectroscopy – a decoherence descriptor for radicals in glassy matrices. *Physical Chemistry Chemical Physics*, 23(38):21664–21676, 2021.
- [46] J.J. Sylvester. LX. Thoughts on inverse orthogonal matrices, simultaneous signsuccessions, and tessellated pavements in two or more colours, with applications to Newton’s rule, ornamental tile-work, and the theory of numbers. *The London, Edinburgh, and Dublin Philosophical Magazine and Journal of Science*, 34(232):461–475, 1867.
- [47] Zhecheng Sun, Weibin Ni, Denan Li, Xiya Du, Aimei Zhou, Shi Liu, and Lei Sun. Ultralong room-temperature qubit lifetimes of covalent organic frameworks. *Journal of the American Chemical Society*, 147(35):31930–31939, 2025.
- [48] Wen Yang and Ren-Bao Liu. Universality of Uhrig dynamical decoupling for suppressing qubit pure dephasing and relaxation. *Physical Review Letters*, 101(18):180403, 2008.
- [49] Götz S. Uhrig. Keeping a quantum bit alive by optimized π -pulse sequences. *Physical Review Letters*, 98(10):100504, 2007.
- [50] John P. Mugler. Optimized three-dimensional fast-spin-echo MRI. *Journal of Magnetic Resonance Imaging*, 39(4):745–767, 2014.

Acknowledgements

This work was supported by the National Natural Science Foundation of China (grant No. 22273078 and No. T2125011), the Hangzhou Municipal Funding Team of Innovation (TD2022004), and the Chinese Academy of Sciences (grant No. YSBR-068). W.N. and L.S. acknowledge CIQTEK Co., Ltd., Quantum Inspire, and the Instrumentation and Service Center for Molecular Sciences at Westlake University for facility support and technical assistance. W.N. and L.S. acknowledge Dr. Zhifu Shi for providing molecular qubits, Qian Cao for preliminary theoretical studies, Junfeng Wu, Dr. Zhichao Liu, and Dr. Mengxiang Zhang for assistance with experiments on trapped ion qubits, Marios Samiotis from Dicarolo laboratory for assistance with experiments on superconducting transmon qubits, and Dr. Maria Grazia Concilio and Prof. Xueqian Kong for preliminary simulations. W.N. acknowledges Dr. Aimei Zhou and Zhiyang Wang for assistance with pulse EPR spectroscopy, Jiaqi Han, Prof. Jian Li, and Prof. Huayi Chen for helpful discussions, and Yingchao Wang and Xiaoqing Yuan for assistance with artistic design. L.S. acknowledges Prof. Tijana Rajh, Dr. Tianxing Zheng, Prof. Dafei Jin, Prof. Xinhao Li, Dr. Ralph T. Weber, and Dr. Yutian Wen for helpful discussions.

Author contributions

L.S. and W.N. conceived the idea, designed experiments, and oversaw the project. W.N. conducted theoretical analysis, proposed HPC and its benchmark, and performed experiments on trapped ion, superconducting, and molecular qubits. Z. L., G.Q., and F.S. performed experiments on NV centers in diamond, and W.N. assisted with these experiments. Z.S. synthesized Cu^{2+} -based molecular qubits. J.D. assisted with theoretical analysis regarding orthogonality ratio. W.N. and L.S. co-wrote the manuscript. All authors have given approval to the final version of the manuscript.

Competing interests

The authors declare that they have no competing interests.

Materials & correspondence

Correspondence and requests for materials should be addressed to Lei Sun.

Supplementary Information for Scalable quantum error mitigation with phase-cycled dynamical decoupling

1 Introduction

1.1 Problem setup

We consider a two-level quantum system (qubit) subject to pure dephasing errors. Without loss of generality, one can imagine it as an ensemble of electron spins ($S = \frac{1}{2}$) under a static and strong quantizing magnetic field B_0 along the z -axis, with pure dephasing errors described by the on-site disorder:

$$H = (\omega + \delta\omega_i(t))\hat{S}_z, \quad (1)$$

where $\delta\omega_i(t) \ll \omega$ and $\omega = g_e\mu_B\hbar^{-1}B_0$ is unperturbed Zeeman splitting with g_e , μ_B , \hbar , \hat{S}_z representing the g -factor of the electron spin, Bohr magneton, reduced Planck constant, and a Pauli- z matrix, respectively. We further assume that all spin-spin interaction terms are negligible such that \hat{S}_z is the only non-trivial term.

Due to the negligible spin-spin interactions, we focus on a single spin in the rotating frame for our analysis, where the first term $\omega\hat{S}_z$ can be omitted. The system's state is fully described by the 2×2 density matrix ρ . We assume the initial state to be:

$$\rho(0) = \begin{pmatrix} 1 & 0 \\ 0 & 0 \end{pmatrix}. \quad (2)$$

In general, the qubit's density matrix reads:

$$\rho = \begin{pmatrix} P_0 & C_+ \\ C_- & P_1 \end{pmatrix}, \quad (3)$$

where

- P_0 and P_1 represent populations of states $|0\rangle$ and $|1\rangle$, respectively, with $P_0 = 1 - P_1$;
- C_+ and C_- are complex conjugates ($C_- = C_+^*$) encoding the coherence between $|0\rangle$ and $|1\rangle$.

To understand why coherence-population mixing matters, we add longitudinal relaxation characterized by T_1 and transverse relaxation characterized by T_2 :

$$\rho(t) = \begin{pmatrix} 1 - P_1 e^{-t/T_1} & C_+ e^{-i\delta\omega t} e^{-t/T_2} \\ C_- e^{i\delta\omega t} e^{-t/T_2} & P_1 e^{-t/T_1} \end{pmatrix}. \quad (4)$$

Equivalently, the density matrix can be represented as:

$$\rho(t) = \frac{1}{2} \left[\hat{S}_0 + (1 - 2P_1 e^{-t/T_1}) \hat{S}_z + C_+ e^{-i\delta\omega t - t/T_2} \hat{S}_+ + C_- e^{i\delta\omega t - t/T_2} \hat{S}_- \right]. \quad (5)$$

An ideal inversion pulse would exchange populations ($P_0 \leftrightarrow P_1$) and swap coherences ($C_+ \leftrightarrow C_-$) with a phase factor. However, imperfect (noisy) inversion pulses introduce coherence-population mixing, generating spurious signals like stimulated echoes that adversely affect coherence measurements.

The density matrix can be represented by a linear combination of a complete basis. The most commonly used basis set is $\{\hat{S}_0, \hat{S}_x, \hat{S}_y, \hat{S}_z\}$, where \hat{S}_0 is the two-dimensional identity matrix and $\hat{S}_{x,y,z}$ are Pauli matrices. Here, we choose $\{\hat{S}_0, \hat{S}_+, \hat{S}_-, \hat{S}_z\}$ because these terms explicitly represent coherence and population. It allows straightforward calculation of the free evolution with pure dephasing:

$$\begin{aligned} \hat{S}_0(t) &= \hat{S}_0(0), \\ \hat{S}_z(t) &= \hat{S}_z(0), \\ \hat{S}_+(t) &= \hat{S}_+(0) e^{-i\delta\omega t}, \\ \hat{S}_-(t) &= \hat{S}_-(0) e^{+i\delta\omega t}, \end{aligned} \quad (6)$$

where $\hat{S}_\pm = \frac{1}{2}(\hat{S}_x \pm i\hat{S}_y)$. We can then define coherence orders $p = \pm 1, 0$:

$$\hat{S}_p(t) = \hat{S}_p(0) e^{-ip\delta\omega t}. \quad (7)$$

Note that

$$\hat{S}_+ = \begin{pmatrix} 0 & 1 \\ 0 & 0 \end{pmatrix}, \hat{S}_- = \begin{pmatrix} 0 & 0 \\ 1 & 0 \end{pmatrix}, \frac{\hat{S}_0 + \hat{S}_z}{2} = \begin{pmatrix} 1 & 0 \\ 0 & 0 \end{pmatrix}, \frac{\hat{S}_0 - \hat{S}_z}{2} = \begin{pmatrix} 0 & 0 \\ 0 & 1 \end{pmatrix}. \quad (8)$$

Evidently, $p = \pm 1$ represent coherence, and $p = 0$ represents population (see equation (3)). For simplicity, we drop the identity term in the following analysis.

1.2 Hahn echo

The above basis enables calculation of the most well-known spin echo, namely Hahn echo, generated by a $\pi/2$ pulse followed by an inversion pulse (π pulse):

$$\hat{S}_z \xrightarrow{(\frac{\pi}{2})_y} \frac{\hat{S}_+ + \hat{S}_-}{2} \xrightarrow{\tau} \frac{\hat{S}_+ e^{-i\delta\omega\tau} + \hat{S}_- e^{i\delta\omega\tau}}{2} \xrightarrow{(\pi)_x} \frac{\hat{S}_- e^{-i\delta\omega\tau} + \hat{S}_+ e^{i\delta\omega\tau}}{2} \quad (9)$$

After another free evolution time τ , $\frac{\hat{S}_+ + \hat{S}_-}{2}$ reappears, resulting in a Hahn echo. This echo reflects decoherence as it only involves $p = +1$ and $p = -1$ after the $\pi/2$ pulse. Note that $\delta\omega$ is assumed to be constant within time 2τ , and we apply this assumption throughout the following analysis for simplicity. We can also track the coherence order transfer during this process. There are two symmetric pathways: $0 \rightarrow +1 \rightarrow -1$ and $0 \rightarrow -1 \rightarrow +1$. Due to symmetry, we only need to consider one of them as \hat{S}_+ and \hat{S}_- always appear in pairs with equal magnitude.

1.2.1 Conclusion 1: Echo formation condition

The coherence order of the initial state is $p = 0$ according to equation (2) and equation (7). We can then represent the coherence transfer pathways by two series of coherence orders:

$$(0, p_1, p_2, \dots, p_n, -1), (0, -p_1, -p_2, \dots, -p_n, +1). \quad (10)$$

They are symmetric and essentially summarize the same dynamics. The echo formation condition requires the qubit to spend equal time in \hat{S}_+ and \hat{S}_- because all dephasing will be refocused by the inversion pulse according to equation (6).

For free evolution times $(\tau_1, \tau_2, \dots, \tau_n)$ corresponding to each coherence order, if the final coherence order is -1 , the echo occurs at time t after the last pulse when the following condition is satisfied:

$$t = \sum_{i=1}^n p_i \tau_i > 0. \quad (11)$$

This means that the qubit spends more time on $p = +1$ than $p = -1$, so that it needs some extra time on $p = -1$ to form an echo. If the final coherence order is $+1$, then t has to be smaller than 0. Assume that the qubit has evolved according to the first coherence transfer pathway in equation (10). It gains a phase of $e^{-i\delta\omega \sum_{i=1}^n p_i \tau_i} = e^{-i\delta\omega t}$. After free evolution time t on $p = -1$, this extra phase disappears according to equation (6), generating an echo.

1.3 Stimulated echo

The classic pulse sequence generating a stimulated echo is: $(\frac{\pi}{2} - \tau - \frac{\pi}{2} - T - \frac{\pi}{2})$. While there exist numerous coherence transfer pathways, Conclusion 1 immediately reveals that a stimulated echo will appear at time τ after the last pulse, corresponding to the pathway $(0, +1, 0, -1)$ or $(0, -1, 0, +1)$. Pathways that do not form echoes (anti-echoes) are typically much weaker due to decoherence. The formation of stimulated echo involves coherence-population mixing after each pulse, so the dynamics of this echo reflects both decoherence and longitudinal relaxation.

1.3.1 Conclusion 2: Phase shift of signal

Note the i^{th} pulse induces a change in the coherence order Δp_i , and a phase change $\Delta \phi_i$ in the i^{th} pulse causes a phase shift in the final signal. Accordingly, the total phase shift $\Delta \Phi$ in the final signal is:

$$\Delta \Phi = \sum_i \Delta p_i \Delta \phi_i. \quad (12)$$

In this context, all phases are defined as the angle with respect to $+x$ axis. For example, a pulse along $+y$ has a $\frac{\pi}{2}$ phase, and the corresponding single qubit rotation is along $+y$ axis. An echo with phase $+y$ means the echo appears at $+y$ axis. In our setup, $\Delta p \in \{0, \pm 1, \pm 2\}$ and $\Delta \phi \in \{0, \pi\}$. This implies that changing a pulse's phase introduces a π phase shift to the final signal only when $\Delta p = \pm 1$. The coherence transfer pathways can thus be classified by the number of $\Delta p = \pm 1$ transitions. This classification aligns perfectly with our goal of distinguishing population and coherence. For k phase-flipped pulses:

- Even k : No change in the final signal ($\Delta \Phi = 0$)
- Odd k : Final signal gains a minus sign (π phase shift, i.e. $\Delta \Phi = \pi$)

These properties form the foundation of phase cycling design for inversion-pulse-based dynamical decoupling (IDD).

1.4 Phase cycling

Phase cycling enables selection of desired coherence transfer pathways and corresponding echoes. A noisy pulse could cause all possible coherence order transfers, and an N -pulse sequence can possibly generate $\frac{1}{2}(3^{N-1} - 1)$ echoes, making the phase cycling of dynamical decoupling sequences complicated.

Take CPMG- m sequence as an example, which includes a $\pi/2$ pulse followed by m spin-locking inversion pulses with equal intermittent free evolution times. We first consider the CPMG-2 sequence with fixed final coherence order $p = -1$ to show the principle of phase cycling. There are 4 coherence transfer pathways that could generate echoes after the last pulse as summarized in Table 1.

p_0	p_1	p_2	p_3	Echo Position
0	-1	+1	-1	τ
0	+1	+1	-1	3τ
0	0	+1	-1	2τ
0	+1	0	-1	τ

Table 1: Coherence transfer pathways in CPMG-2. Echo position is with respect to the last pulse.

The desired pathway $(0, -1, +1, -1)$ representing qubit coherence overlaps with $(0, +1, 0, -1)$ (stimulated echo). Phase cycling resolves this issue: the desired echo is an one-pulse echo while the stimulated echo is a three-pulse echo, distinguished by the number of $\Delta p = \pm 1$ transitions within their pathways (Table 2). Later we will see such a classification allows us to analyze $\frac{1}{2}(3^{N-1} - 1)$ echoes in an elegant way. In this case, by performing two experiments, where one of them flips either inversion pulse with respect to the other experiment, and summing the final signals, the stimulated echo cancels out while the desired echo doubles (see Table 3 for a more complex phase cycling that involve four experiments).

Δp_0	Δp_1	Δp_2	Δp_3	Echo Position
<i>None</i>	-1	+2	-2	τ
<i>None</i>	+1	-1	-1	τ

Table 2: Changes of coherence orders in CPMG-2

1.5 Phase cycling problem in CPMG

Recall that a coherence transfer pathway can be represented as:

$$(0, p_1, p_2, \dots, p_{m+1}, -1).$$

The key to designing the phase cycling for CPMG- m is to exclude $p_i = 0$ within the coherence transfer pathway because we should probe pure decoherence processes ($p_i = \pm 1$) without

Sign	Pulse 1	Pulse 2	Pulse 3	Desired echo	Stimulated Echo
+	+X	+Y	+Y	Original	Original
+	+X	+Y	-Y	Original	Flipped
+	+X	-Y	+Y	Original	Flipped
+	+X	-Y	-Y	Original	Original

Table 3: Complete phase cycling for CPMG-2. The symbol in the “Sign” column indicates addition or subtraction of the final signal. “Original” and “Flipped” represent phases of echoes.

involving the longitudinal relaxation. Our objective then reduces to eliminating $\Delta p = \pm 1$ transitions, which are generated by imperfect inversion pulses, except for the first $\pi/2$ pulse that prepares the coherence.

Consider the stimulated echo in the example of phase cycling in Table 3. Denote the original pulse phases (the first row) to be $[+1, +1, +1]$. These pulses produce the final signal with the original phase. Phase flipping of any pulse ($+1$ to -1 , i.e. $\Delta\phi_i = \pi$) inverts the signal sign, producing a π phase shift of the final signal. Critically, the phase of the final signal is determined by the product of all pulse phases. For instance:

- $[+1, +1, -1]$ and $[+1, -1, +1]$ yield the final signal with a π phase shift;
- $[+1, -1, -1]$ gives the final signal with the original phase.

Denote the original and π phase-shifted signals as $+1$ and -1 , respectively. The sum of results of the four phase cycling steps is $+1 + (-1) + (-1) + 1 = 0$, confirming that the phase cycling cancels out the three-pulse echo, i.e. stimulated echo. In contrast, the desired echo is amplified because the phase of the first $\pi/2$ pulse is not flipped. Consequently, we can transform the design principle of phase cycling into an orthogonality condition that is concisely expressed as:

$$\begin{pmatrix} +1 \\ +1 \\ +1 \\ +1 \end{pmatrix} \circ \begin{pmatrix} +1 \\ +1 \\ -1 \\ -1 \end{pmatrix} \circ \begin{pmatrix} +1 \\ -1 \\ +1 \\ -1 \end{pmatrix} = \begin{pmatrix} +1 \\ -1 \\ -1 \\ +1 \end{pmatrix}. \quad (13)$$

Here, “ \circ ” denotes the Hadamard product, i.e. the element-wise product. The orthogonality requires the summation of all elements in the result vector to be zero. In this case, three-vector orthogonality translates to the cancellation of the three-pulse echo. As the phase of the desired echo is exclusively determined by the the phase of the first $\pi/2$ pulse, this orthogonality condition is applicable to all IDD sequences.

2 Phase Cycling Scheme

2.1 Basic definitions

Define a phase cycling set:

$$G \subseteq V_N, \quad G = \{g_1, g_2, \dots, g_n\} \cup \{E\} \quad (14)$$

where V_N is an N -dimensional vector space, each g_i contains equal numbers of $+1$ and -1 elements, and E is an all-one vector. The phase cycling matrix comprises elements from this set that are used as column vectors. Each row of this matrix represents phases of all pulses within the sequence in one phase cycling step, and each column represents the phase configuration of one pulse throughout all phase cycling steps.

Define Hadamard product orthogonality (HPO) of k column vectors in G if they fulfill the following condition:

$$g_1 \circ g_2 \circ \dots \circ g_k = g_i \neq E. \quad (15)$$

As the sum of all elements in g_i is equal to 0, this condition leads to the cancellation of k -pulse echoes.

2.2 Complete phase cycling (CPC)

2.2.1 Construction

We now prove that CPC for IDD- m , where m represents the number of inversion pulses, is possible by giving one construction directly. By definition, CPC mitigates all control errors—it cancels all k -pulse echoes for any $1 \leq k \leq m$, except for the desired echo. It is equivalent to constructing a matrix in which any subset of column vectors satisfies HPO. At present, we assume that the first $\pi/2$ pulse's phase is always $+1$ and focus on inversion pulses.

We construct a matrix encompassing all phase configurations of m inversion pulses. Each pulse has two phase choices, ± 1 . Accordingly, the matrix shape is $(2^m, m)$. This matrix can be represented as:

$$M = \{g_1, g_2, g_3, \dots, g_m\}. \quad (16)$$

We can easily check that any subset $K = \{g_{k_1}, g_{k_2}, \dots, g_{k_k}\}$ of M satisfies HPO, which requires half elements of the result vector $g_i = g_{k_1} \circ g_{k_2} \circ \dots \circ g_{k_k}$ equal to $+1$. Denote the number of $+1$ as $N(+1)$ and the number of -1 as $N(-1)$. The k vectors give rise to 2^k phase configurations, which are repeated 2^{m-k} times in the subset K . Therefore, we only need to

consider one of the repetitions. Imagine k pulses whose phases are all initially $+1$. We can choose $0 \leq j \leq k$ of them to become -1 , which gives rise to 2^k possible constructions of row vectors of the subset K . If we chose an even number of the original row to become -1 , the product of all elements within the resulting row would be $+1$. If we chose an odd number of the original row to become -1 , the product would be -1 . We thus have:

$$\begin{aligned} N(+1) &= \sum_{\text{even}} C_k^{\text{even}}, \\ N(-1) &= \sum_{\text{odd}} C_k^{\text{odd}}. \end{aligned} \tag{17}$$

$N(+1)$ equals to $N(-1)$ because:

$$\begin{aligned} (-1 + 1)^k &= C_k^0(-1)^k + C_k^1(-1)^{k-1} + \dots + C_k^k(-1)^0 \\ &= \left(\sum_{\text{even}} C_k^{\text{even}} - \sum_{\text{odd}} C_k^{\text{odd}} \right) (-1)^k = 0 \end{aligned} \tag{18}$$

Therefore, any subset of M satisfies HPO. Namely, M represents CPC.

2.2.2 Complexity

While theoretically elegant, CPC becomes impractical for large m , requiring 2^m experiments. We prove that this is the minimal requirement.

Assume that M' is a CPC matrix (N, m) consisting of $\{g_1, g_2, \dots, g_m\}$. For any $i \neq j$, $g_i \circ g_j \notin M'$, because if $g_i \circ g_j = g_k \in M'$, then $g_i \circ g_j \circ g_k = g_k \circ g_k = E$, which is inconsistent with the property of CPC. Hence, $g_i \circ g_j$ results in a new element. It is orthogonal to any element in M' because $g_k \circ g_i = g_j$, $g_k \circ g_j = g_i$, and g_k and any other element in M' must fulfill HPO according to the property of CPC. We can construct C_m^2 such new elements. Similarly, they are orthogonal to each other. All new elements plus the original M' form a matrix whose all column vectors are mutually orthogonal. For same reasons, we can also group 3, 4, \dots , m elements together, and finally construct a much bigger matrix whose number of columns is:

$$C_m^1 + C_m^2 + C_m^3 + \dots + C_m^m = (1 + 1)^m - C_m^0 = 2^m - 1 \tag{19}$$

Note that we can always add E as the first column of the matrix, so finally we have 2^m elements. At this point, all the elements are still mutually orthogonal; equivalently, they are linearly independent. Therefore, the number of rows of the matrix (dimension of the present vector space) must be larger than or equal to the number of columns (dimension of the set of linearly independent vectors). Finally, we have:

$$N \geq 2^m. \tag{20}$$

Table 4: Example of CPC for CPMG-4

Pulse 1	Pulse 2	Pulse 3	Pulse 4
+	+	+	+
+	+	+	-
+	+	-	+
+	+	-	-
+	-	+	+
+	-	+	-
+	-	-	+
+	-	-	-
-	+	+	+
-	+	+	-
-	+	-	+
-	+	-	-
-	-	+	+
-	-	+	-
-	-	-	+
-	-	-	-

Note: Consider a subset $K = \{g_3, g_4\}$. Regarding the last two pulses, the first four rows already contain all possible phase configurations, and the rest of rows are simply their repetitions.

The complexity of CPC is at least 2^m . The construction of CPC in Section 2.2.1 is optimal.

Experimental Consideration: While theoretically setting the first pulse's phase to E suffices, practical implementations often phase cycling the first pulse as $\begin{pmatrix} E \\ -E \end{pmatrix}$ to eliminate baseline drift. This is actually a combination of CPC and two-step phase cycling (TPC). Fortunately, we can now set the first inversion pulse's phase to be E because it does not cause any unwanted signal if we neglect anti-echoes. So, the complexity is still 2^m .

2.3 Hadamard phase cycling (HPC)

Since CPC has exponential complexity $\mathcal{O}(2^m)$, it is meaningful to design a good approximate phase cycling matrix that eliminates as many unwanted signals as possible while maintaining as low complexity as possible. Here, we show that regarding IDD- m sequences, HPC has only

linear complexity $\mathcal{O}(m)$ while canceling out more than 98% unwanted signals for $m > 16$.

2.3.1 Sylvester's construction of Hadamard matrix

Hadamard matrix is a square matrix of elements $+1$ and -1 , where any two columns of the matrix are orthogonal: $H^T H = nI$.

Mathematicians suspect that any Hadamard matrix of order $4n$ always exists, where n is an integer. This Hadamard conjecture remains unproved, but there exist many methods to construct Hadamard matrix. Here, we use Sylvester's method to construct Hadamard matrix of order 2^n :

$$H_{2^n} = \begin{pmatrix} H_{2^{n-1}} & H_{2^{n-1}} \\ H_{2^{n-1}} & -H_{2^{n-1}} \end{pmatrix}, H_1 = (1). \quad (21)$$

Note that this matrix's first column is always an all-one vector, and due to its original orthogonality, it automatically mitigates all stimulated echoes that overlap with the desired echoes of CPMG.

2.3.2 Phase cycling group

Represent Sylvester's Hadamard matrix as $H = \{E, g_1, g_2, \dots, g_H\}$ like previous discussions. This set is an abelian group under Hadamard product, resulting in great HPO that means although not all subsets of the phase cycling matrix satisfy HPO, a significantly large ratio of subsets do satisfy.

Note that an abelian group requires the elements to satisfy these five properties:

Closure: $\forall g_i, g_j \in H; g_i \circ g_j \in H$.

Identity Existence: $\forall g, \exists E; g \circ E = E \circ g = g$.

Inverse Existence: $\forall g, \exists g^{-1}; g \circ g^{-1} = g^{-1} \circ g = E$.

Associative law: $\forall g_i, g_j, g_k \in H, (g_i \circ g_j) \circ g_k = g_i \circ (g_j \circ g_k)$.

Commutative law: $\forall g_i, g_j \in H, g_i \circ g_j = g_j \circ g_i$.

Hadamard product is essentially a multiplication, so it automatically satisfies the associative law and the commutative law. The identity in H is E , which consists of only $+1$ elements. The inverse of an element is just itself. Here, we prove the closure of H . First, notice that

H_2 obviously satisfies the closure. Based on the Sylvester's construction of H_4 from H_2 , the new elements in H_4 also satisfy the closure because they are formed by stacking elements in H_2 . Similar logic is applicable to any higher-order matrix. In fact, one can treat $\begin{pmatrix} H & H \\ H & -H \end{pmatrix}$ as some kind of H_2 , then the closure becomes obvious.

$$H_2 = \begin{pmatrix} 1 & 1 \\ 1 & -1 \end{pmatrix}, H_4 = \begin{pmatrix} 1 & 1 & 1 & 1 \\ 1 & -1 & 1 & -1 \\ 1 & 1 & -1 & -1 \\ 1 & -1 & -1 & 1 \end{pmatrix}. \quad (22)$$

2.3.3 Great Hadamard product orthogonality

We now prove the great HPO of the phase cycling group. We first prove a conclusion to give some intuitions of the phase cycling group's great HPO:

$$\begin{aligned} g_1 \circ g_2 \circ \cdots \circ g_{i-1} \circ g_i &= E \\ g_1 \circ g_2 \circ \cdots \circ g_{i-1} &= E \circ g_i \\ g_1 \circ g_2 \circ \cdots \circ g_{i-1} \circ g_j &= E \circ g_i \circ g_j \\ g_i \circ g_j &= g_k \neq E \end{aligned} \quad (23)$$

Accordingly, if we had i elements that do not satisfy HPO, we would be able to change any one of them to another element beyond the original set to construct a new set whose elements satisfy HPO.

We now discuss the proportion of the number of combinations of elements that do not satisfy HPO. Assume that we have 2^n elements in the phase cycling group G_H , and pick q elements from $G_H - \{E\}$. Define $p(q)$ as the probability that these elements do not satisfy HPO, and define $D(q)$ as the number of combinations satisfying $g_1 \circ g_2 \cdots \circ g_q = E$, where $1 \leq q \leq 2^n - 1$.

We have:

$$p(q) = \frac{D(q)}{C_{2^n-1}^q}. \quad (24)$$

Due to the definition of G_H , $p(1) = p(2) = 0$.

When $q = 3$, we need the three elements to satisfy $g_3 = g_1 \circ g_2 \neq E$. Given two elements, then the third element is uniquely determined. However, there are double counting issues while choosing the third element (we have to determine which one of the three elements is the third element), finally:

$$D(3) = \frac{C_{2^n-1}^2}{C_3^1}. \quad (25)$$

When $q = 4$, we need the elements to satisfy $g_4 = g_1 \circ g_2 \circ g_3 \neq E$. Again, given three elements, the fourth element is uniquely determined. Moreover, we have to subtract $D(3)$ combinations satisfying $g_1 \circ g_2 \circ g_3 = E$, because in this case, g_4 would have to be E to satisfy our requirement, which is impossible. Taking the double counting issue into account, we have:

$$D(4) = \frac{C_{2^n-1}^3 - D(3)}{C_4^1}. \quad (26)$$

When $q = 5$, we need the elements to satisfy $g_5 = g_1 \circ g_2 \circ g_3 \circ g_4 \neq E$. Again, given four elements, the fifth element is uniquely determined. Furthermore, we have to subtract combinations satisfying $g_1 \circ g_2 \circ g_3 \circ g_4 = E$ for same reasons as $q = 4$ case. In addition, when $g_1 \circ g_2 \circ g_3 \circ g_4 \neq E$, we need to subtract combinations satisfying $g_1 \circ g_2 \circ g_3 = E$ because this leads to an impossible relation, $g_4 \circ g_5 = E$. Similarly, we have $D(4)$ combinations for the former one. For the latter one, we have $D(3)$ combinations for g_1, g_2, g_3 , and $2^n - 1 - 3$ choices for the fourth elements. Finally:

$$D(5) = \frac{C_{2^n-1}^4 - D(4) - (2^n - 1 - 3)D(3)}{C_5^1}. \quad (27)$$

In fact, the situation of $q = 5$ includes all necessary conditions. Hence, we can consider the general case, i.e. $q \geq 5$ elements satisfying $g_1 \circ g_2 \circ \cdots \circ g_q = E$. Given $q - 1$ elements, we need to subtract $D(q - 1)$ combinations for $g_1 \circ g_2 \circ \cdots \circ g_{q-1} = E$, and then subtract $(2^n - 1 - q + 2)D(q - 2)$ combinations for $g_1 \circ g_2 \circ \cdots \circ g_{q-2} = E$. We thus have:

$$\begin{aligned} D(q) &= \frac{C_{2^n-1}^{q-1} - D(q-1) - (2^n - q + 1)D(q-2)}{C_q^1}, \\ p(q) &= \frac{1 - p(q-1) - (q-1)p(q-2)}{2^n - q}. \end{aligned} \quad (28)$$

It is straightforward to check that only $q = 1$ violates this relation, but it is a trivial case with $D(1) = p(1) = 0$. Besides, $D(q) = D(2^n - 1 - q)$ because $g_1 \circ g_2 \circ \cdots \circ g_{2^n-1} = E$.

We continue to derive the general formula for $D(q)$ and $p(q)$ based on the recursive formula. First, we prove a lemma:

$$p(2k) = p(2k - 1). \quad (29)$$

When $k = 1$, $p(2) = p(1) = 0$. When $k = l$, assume that $p(2l) = p(2l - 1)$. Hence, when $k = l + 1$, using equation (28):

$$\begin{aligned} (2^n - 2l - 1) \times p(2l + 1) &= 1 - p(2l) - 2l \times p(2l - 1), \\ (2^n - 2l - 2) \times p(2l + 2) &= 1 - p(2l + 1) - (2l + 1) \times p(2l). \end{aligned} \quad (30)$$

From these equations, we get:

$$p(2(l+1)) = p(2(l+1) - 1). \quad (31)$$

We thus prove the lemma.

For $q = 2k + 1$:

$$\begin{aligned} D(2k+1) &= \frac{C_{2^{n-1}}^{q-1} - D(q-1) - (2^n - q + 1)D(q-2)}{q} \\ &= \frac{C_{2^{n-1}}^{q-1}}{q} - \frac{(2^n - q + 1)D(q-2)}{q-1}. \end{aligned} \quad (32)$$

Write $\frac{C_{2^{n-1}}^{q-1}}{q}$ as $\frac{C_{2^{n-1}}^q}{2^n} + \frac{(2^n - q + 1)C_{2^{n-1}}^{q-2}}{(q-1)2^n}$, and change q to $2k + 1$:

$$D(2k+1) - \frac{C_{2^{n-1}}^{2k+1}}{2^n} = -\frac{2^{n-1} - k}{k} \left[D(2k-1) - \frac{C_{2^{n-1}}^{2k-1}}{2^n} \right]. \quad (33)$$

Use this relation and $D(1) = 0$, we finally get:

$$D(2k+1) = \frac{C_{2^{n-1}}^{2k+1}}{2^n} + (-1)^{k+1} \times \frac{(2^n - 1)C_{2^{n-1-1}}^k}{2^n}. \quad (34)$$

Similarly:

$$D(2k) = \frac{C_{2^{n-1}}^{2k}}{2^n} + (-1)^k \times \frac{(2^n - 1)C_{2^{n-1-1}}^k}{2^n}. \quad (35)$$

For $p(q)$, we have:

$$\begin{aligned} p(2k) &= \frac{1}{2^n} + (-1)^k \times \frac{2^n - 1}{2^n} \times \frac{C_{2^{n-1-1}}^k}{C_{2^{n-1}}^{2k}}, \\ p(2k+1) &= \frac{1}{2^n} + (-1)^{k+1} \times \frac{2^n - 1}{2^n} \times \frac{C_{2^{n-1-1}}^k}{C_{2^{n-1}}^{2k+1}}. \end{aligned} \quad (36)$$

Theoretically, for an IDD sequence with 32 inversion pulses, CPC requires $2^{32} = 4,294,967,296$ steps, while the phase cycling based on Hadamard matrix only requires 32 steps. The HPO ratio, which is defined as $1 - \sum_k \frac{D(k)}{C_{2^{n-1}}^k}$, is 96.88%.

2.3.4 Final phase cycling scheme

We further improve the HPO ratio by harnessing the parity of coherence transfer pathways and TPC. Note that the Sylvester's Hadamard matrix has extra freedoms to create new

Hadamard matrices. For example, if we change the first column from E to $-E$, the matrix is still a Hadamard matrix with great HPO. We can also add a minus sign to all the rest columns as well, i.e. changing $H' \rightarrow -H'$, to construct a new stacked Hadamard matrix:

$$\begin{pmatrix} E & H' \\ E & -H' \end{pmatrix}. \quad (37)$$

The advantage of this new matrix is that any odd number of elements excluding the first column satisfy HPO. Formally, if q is an odd number, $D(q) = 0$. Imagine that there are odd number of elements in H' forming an unwanted signal; namely, these elements do not satisfy HPO. The Hadamard product of these elements in $-H'$ has an opposite sign. Thus, adding these two Hadamard products together would satisfy HPO. Such stacking increases the HPO ratio from 96.88% to 98.44% for IDD-32. Finally, we can add a column for the first $\pi/2$ pulse to construct HPC:

$$\begin{pmatrix} + & E & E & H' \\ + & E & E & -H' \\ - & -E & E & H' \\ - & -E & E & -H' \end{pmatrix}. \quad (38)$$

Note that we do not need the first two columns to satisfy HPO if we neglect anti-echoes. For IDD- m , we need $4 \times N_{HPC}$ phase cycling steps, where $N_{HPC} = 2^{integer}$ is the smallest number satisfying $N_{HPC} \geq m$. For example, HPC needs 128 phase cycling steps for IDD-32, but it needs 256 phase cycling steps for IDD-34. In sharp contrast, CPC would need 4, 294, 967, 296 and 17, 179, 869, 184 steps for IDD-32 and IDD-34, respectively, both of which are clearly not practical.

Overall, whereas CPC has a complexity of $\mathcal{O}(2^m)$ for IDD- m , HPC significantly reduces the complexity to $\mathcal{O}(m)$ while preserving near-quantitative HPO ratio. HPC is both scalable and effective.

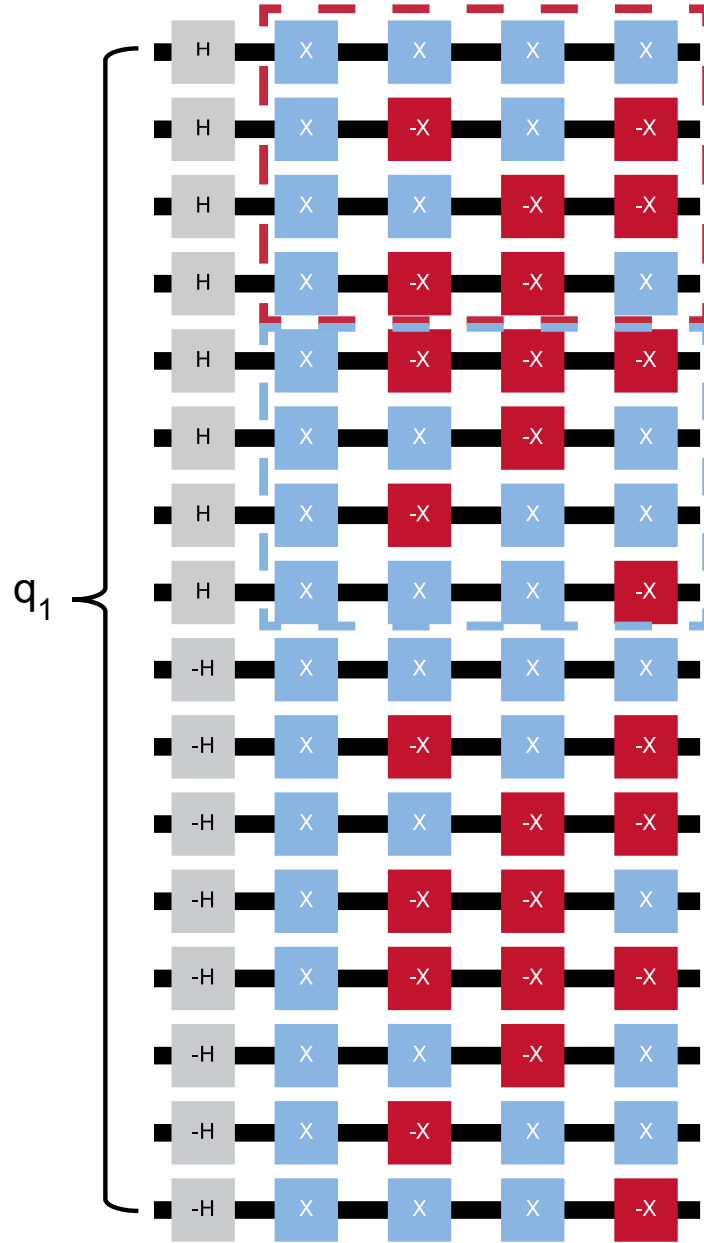


Figure S1. Hadamard phase cycling for IDD-4. q_1 and H represent qubit and Hadamard gate ($\pi/2$ gate), respectively. $\pm X$ represent inversion pulses with opposite phases. Phase configurations within red block represent the original Hadamard matrix, and phase configurations within blue block represent a minus Hadamard matrix except for the first column.

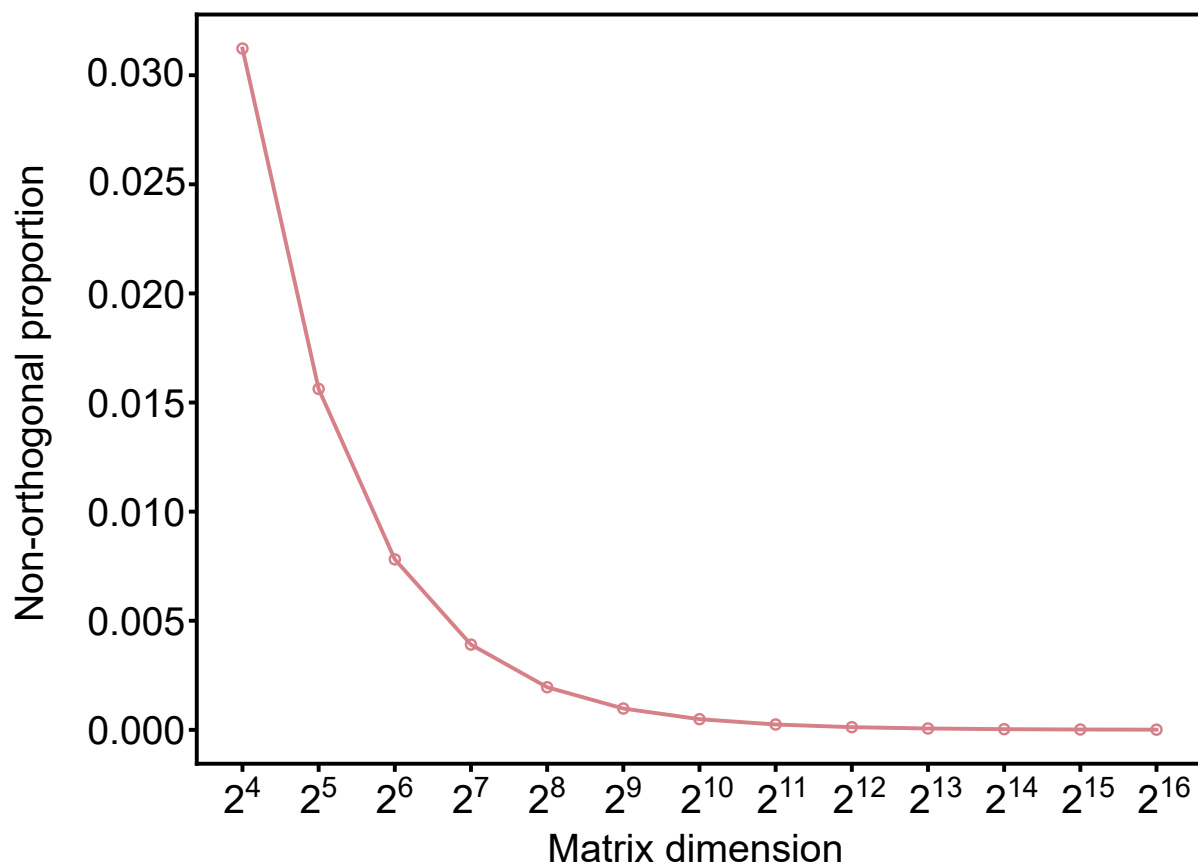


Figure S2. Non-orthogonal ratio (1-HPO ratio) of HPC with different dimensions of Hadamard matrices.

3 Effective State Fidelity

3.1 Definition

State fidelity serves as a merit of how close two quantum states are, which is typically defined as:

$$F(\rho, \sigma) = (\text{Tr} \sqrt{\sqrt{\rho} \sigma \sqrt{\rho}})^2. \quad (39)$$

Here, σ represents the target state and ρ the state for comparison. We define:

$$S_{x,y,z} = \sum_i V_s^i s_{x,y,z}^i \quad (40)$$

$$\langle S_{x,y,z} \rangle = \frac{S_{x,y,z}}{\sqrt{S_x^2 + S_y^2 + S_z^2}},$$

where V_s^i is the i_{th} element of the sign vector (see equation (38)) and $s_{x,y,z}^i$ are expectation values of Pauli operators for the i_{th} phase cycling step. We call $\langle S_{x,y,z} \rangle$ as phase-cycled expectation values and use them to reconstruct the effective quantum state:

$$\rho^{eff} = \frac{1}{2}(\hat{S}_0 + \langle S_x \rangle \hat{S}_x + \langle S_y \rangle \hat{S}_y + \langle S_z \rangle \hat{S}_z). \quad (41)$$

Finally, the effective state fidelity reads

$$F(\rho^{eff}, \sigma) = (\text{Tr} \sqrt{\sqrt{\rho^{eff}} \sigma \sqrt{\rho^{eff}}})^2. \quad (42)$$

The effective state fidelity serves as a useful benchmark for phase cycling. Essentially, phase cycling sums different Bloch vectors, which represent qubit states, to get a more accurate Bloch vector. Thus, the better the phase cycling method, the higher the effective state fidelity (if the DD sequence does not have inherent robustness).

3.2 Shortcomings of robust dynamical decoupling sequences

There are many robust IDD sequences that can fight against control errors, e.g. CPMG, XY-4, XY-8, etc. They share similar essence: compensating previous errors by following pulses. Ironically, such compensations efficiently cause coherence-population mixing. Below is an example of CPMG-2 with longitudinal and transverse relaxations but without dephasing, the latter of which is assumed to be eliminated by IDD. Imagining that we first create a coherence C_+ and let it evolve for time τ , we will get:

$$C_+(\tau) = C_+ e^{-\frac{\tau}{T_2}}. \quad (43)$$

Then we apply a noisy inversion pulse and consider these two terms:

$$\begin{aligned} C_+(\tau) &\rightarrow C'_-(\tau) = C'_- e^{-\frac{\tau}{T_2}}, \\ C_+(\tau) &\rightarrow P'_1(\tau) = P'_1 e^{-\frac{\tau}{T_2}}. \end{aligned} \tag{44}$$

Again, let them evolve for 2τ :

$$\begin{aligned} C'_-(3\tau) &= C'_- e^{-\frac{3\tau}{T_2}}, \\ P'_1(3\tau) &= P'_1 e^{-\frac{\tau}{T_2}} e^{-\frac{2\tau}{T_1}}. \end{aligned} \tag{45}$$

Then we apply another noisy inversion pulse, two possible terms are:

$$\begin{aligned} C'_-(3\tau) &\rightarrow C''_+(3\tau) = C''_+ e^{-\frac{3\tau}{T_2}}, \\ P'_1(3\tau) &\rightarrow C''_-(3\tau) = C''_- e^{-\frac{\tau}{T_2}} e^{-\frac{2\tau}{T_1}}. \end{aligned} \tag{46}$$

In fact, the second term definitely exists for noisy circuits because the conversion from P_1 to C_- is exactly the compensation done by CPMG; namely, this term is the consequence of the robustness. These two processes correspond to $(0, +1, -1, +1)$ and $(0, +1, 0, -1)$ coherence transfer pathways. According to the Conclusion 1, each of them gives rise to an echo after another evolution time τ . The second process clearly introduces longitudinal relaxation into decoherence, resulting in an overestimation of T_2 .

This not only serves as a vivid example of how coherence-population mixing leads to slower decay of the apparent signal, but also points out long-standing yet overlooked shortcomings of robust IDD sequences. Although these sequences can use later pulses to correct previous control errors, these errors still leave influence on the history of dynamics, which possibly distorts tasks such as T_2 acquisition and quantum sensing. Therefore, a non-Markovian quantum error mitigation method is indispensable to correctly probe the intermediate dynamic processes. On the other hand, robust sequences remain useful when the target task does not require correct observation of the intermediate dynamic processes, or when the single-gate fidelity is sufficiently high.

Notably, the way of robust sequences to preserve state fidelity is different from phase cycling. The former only preserve the fidelity of the final state, whereas the latter protects the effective fidelity of every intermediate state. Although one may get a high state fidelity after a robust sequence, the measurement of T_2 may still be incorrect due to erroneous intermediate dynamics.

4 Qubit Platforms

4.1 Ensemble electron spin qubits in molecules

4.1.1 $(\text{PPh}_4)_2[\text{Cu}(\text{mnt})_2]$

The molecular electron spin qubit, $(\text{PPh}_4)_2[\text{Cu}(\text{mnt})_2]$, was synthesized following literature procedure. It was diluted in a diamagnetic isostructural host $(\text{PPh}_4)_2\text{Ni}(\text{mnt})_2$ with a concentration of 0.3% via co-crystallization. Pulse electron paramagnetic resonance (EPR) spectroscopic characterization of this molecule was performed with resonant frequency of 9.6623 GHz under 3340 G magnetic field at 8 K.

4.1.2 COF-5

COF-5 was synthesized from 2,3,6,7,10,11-hexahydroxytriphenylene and benzene-1,4-diboronic acid based on the literature procedure. It hosts semiquinone-like radical qubits derived from partially oxidation of the former linker. It exhibits decent spin dynamic properties at room temperature with $T_1 = 359 \mu\text{s}$ and $T_2 = 1.3 \mu\text{s}$. Pulse EPR spectroscopic characterization of this molecule was performed with resonant frequency of 9.6776 GHz under 3350.5 G magnetic field at 80 K.

4.2 Ensemble electron spin qubits in diamond NV centers

The ensemble NV centers were created by implanting $^{15}\text{N}^+$ ions at an energy of 10 keV, and a dose of $5 \times 10^{12} \text{ cm}^{-2}$. The mean depth of implanted ions is approximately 30 nm. At this depth, the NV centers are sufficiently shielded from surface-induced noise and exhibit spin dynamic properties similar to those of deep NV centers. Prior to experiments, the diamond sample was chemically cleaned in a hot tri-acid mixture ($\text{H}_2\text{SO}_4 : \text{HNO}_3 : \text{HClO}_4 = 1 : 1 : 1$ by volume) at 180 °C.

4.3 Trapped ion qubits

Experiments on trapped ion qubits were conducted on the CIQTEK’s Ion I Quantum Computer, where each $^{40}\text{Ca}^+$ ion was confined in a segmented-blade Paul trap. The qubit was manipulated on the 729 nm optical transition at room temperature, with single-qubit gate fidelity being approximately 0.999. The relaxation time was measured to be $T_1 = 1.0 \text{ s}$ using

the inversion recovery technique. The coherence time was $T_2^{Hahn} = 976 \mu\text{s}$ obtained from Hahn echo decay experiments.

4.4 Superconducting qubits

Experiments on superconducting transmon qubits were conducted on the Quantum Inspire’s Starmon-7 Superconducting Quantum Processor, which consists of seven transmon qubits and is available on the cloud. Each transmon qubit was controlled via dedicated microwave and flux-bias lines for single-qubit and two-qubit gates, and was read out via a dispersively coupled resonator. Each resonator incorporated a Purcell filter and was frequency-multiplexed onto one of two shared feedlines: one for qubits Q0 and Q2, and another for the rest. More detailed information about hardware of Starmon-7 can be found in https://github.com/DiCarloLab-Delft/QuantumInspireUtilities/blob/main/Starmon7_FactSheet.pdf. During our experiments, the single gate fidelity was well above 99%. Detailed information about the processors performance can be found on <https://monitoring.qutech.support/public-dashboards/7171f0e3cfc44995a97dff9001c4d7d1?orgId=1&from=now-7d&to=now>.

5 Methods and Results

5.1 Pulse EPR spectroscopy

X-band (around 9.6 GHz) pulse EPR spectroscopy was performed on a CIQTEK EPR100 spectrometer. The length of π pulse was fixed to be 32 ns for all experiments, determined by nutation experiments.

5.1.1 Inversion recovery measurements

The spin-lattice relaxation time (T_1) was measured using an inversion recovery sequence $\pi - T - \pi/2 - \tau - \pi - \tau - echo$. For all experiments, a four-step phase cycling was employed with pulse phases of $(+x, -x, +x)$, $(+x, +x, +x)$, $(-x, -x, +x)$, and $(-x, +x, +x)$. The resulting echo decay was measured by varying the interval T , and the inversion recovery curve was fitted with a stretched exponential decay function for $(\text{PPh}_4)_2[\text{Cu}(\text{mnt})_2]$ or a double-exponential decay function for COF-5 to extract T_1 .

5.1.2 Hahn echo decay measurements

T_2^{Hahn} was characterized using Hahn echo pulse sequence ($\pi/2 - \tau - \pi - \tau - echo$). Two-step phase cycling was used to cancel baseline drift. The Hahn echo decay was measured by varying the interval τ , and the echo decay curve was fitted with a stretched exponential decay function for $(PPh_4)_2[Cu(mnt)_2]$ or a mono-exponential decay function for COF-5 to extract T_2 .

5.1.3 CPMG measurements

Typical CPMG sequence can be represented as $(\pi_x/2 - [\tau - \pi_y - 2\tau - \pi_y - \tau]_n - echo)$. We conducted two types of CPMG experiments. In the first type, while fixing pulse intervals ($\tau = 120, 150, 400$ ns for NV centers, $(PPh_4)_2[Cu(mnt)_2]$, and COF-5 respectively) and adding pulse number, the echo at time τ after each pulse was collected. In the second type, while fixing the pulse number and increasing the pulse interval, we monitored the decay of the echo at time τ after the last pulse, which can be fitted by a mono-exponential decay function to extract T_2 .

5.1.4 UDD measurements

For UDD- m , the inversion pulses were applied at time $t_n = t \sin^2 \frac{n\pi}{2(m+1)}$, $n = 1, 2, \dots, m$. The desired echo appeared at time t . Similar to CPMG experiments, we also conducted two types of UDD- m experiments. In the first type, while fixing $t = 5000$ ns and adding pulse number, the desired echo after each pulse was collected. In the second type, while fixing the pulse number and increasing t , the decay curve of the desired echo after the last pulse was collected and fitted by a mono-exponential decay function to extract T_2 .

5.2 Optical detected magnetic resonance spectroscopy

Experiments for NV centers in diamond were performed with a homebuilt instrument under a quantizing magnetic field of approximately 315 G. The mono-exponential decay function was used for fitting to extract T_1 and T_2 .

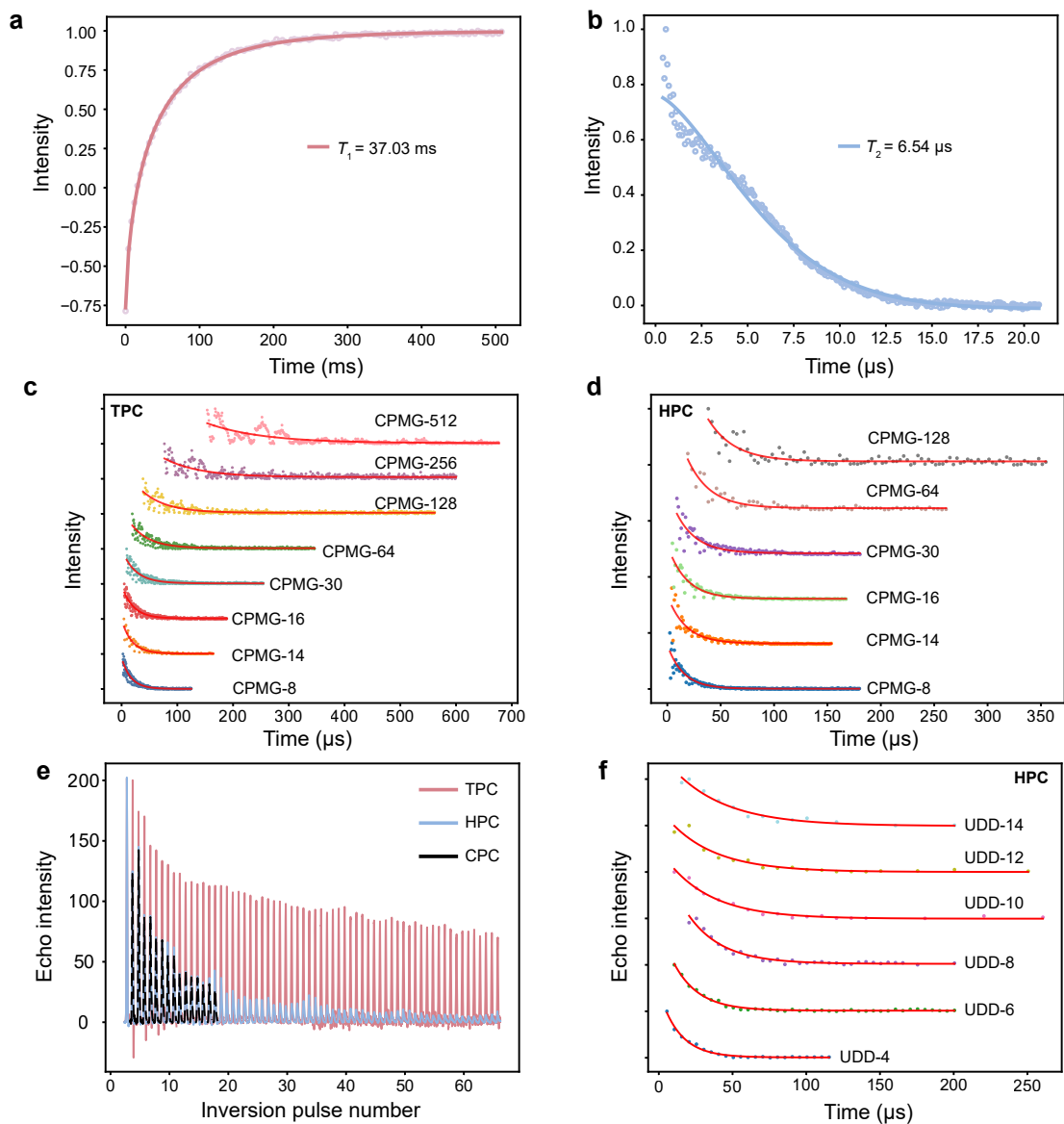


Figure S3. Pulse EPR spectroscopic characterization results of $(\text{PPh}_4)_2[\text{Cu}(\text{mnt})_2]$ at 8 K. **a**, inversion recovery curve. **b**, Hahn echo decay curve. **c,d**, echo decay curves for CPMG experiments with TPC and HPC, respectively. **e**, comparison between echoes collected under CPMG with different phase cycling methods. **f**, echo decay curves for UDD experiments with HPC.

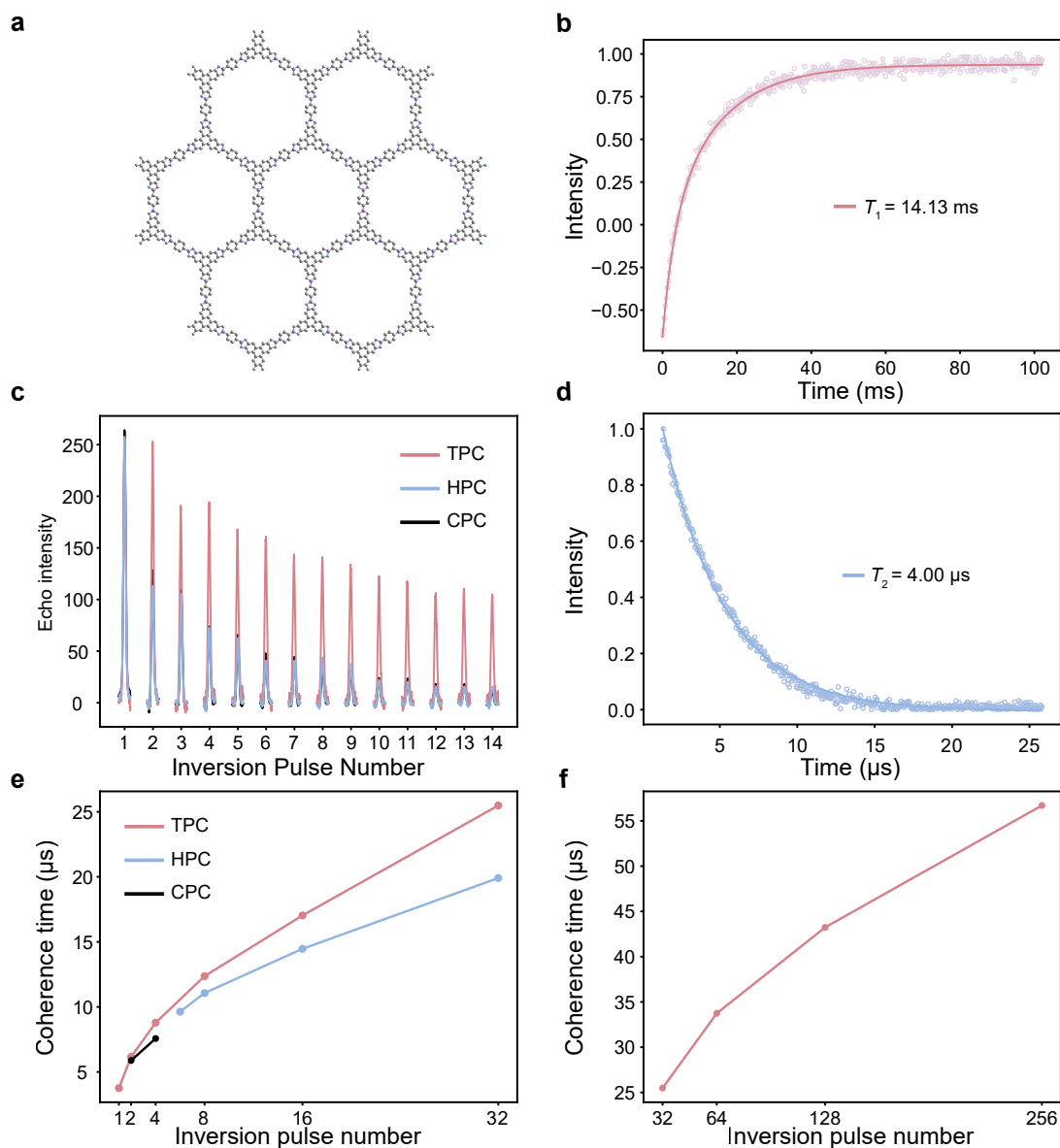


Figure S4. Pulse EPR spectroscopic characterization results of COF-5 at 80 K. **a**, structure of COF-5. **b**, inversion recovery curve. **c**, comparison between echoes collected under CPMG with different phase cycling methods. **d**, Hahn echo decay curve. **e**, comparison between T_2 measured by CPMG with different phase cycling methods. **f**, T_2 measured by CPMG with TPC.

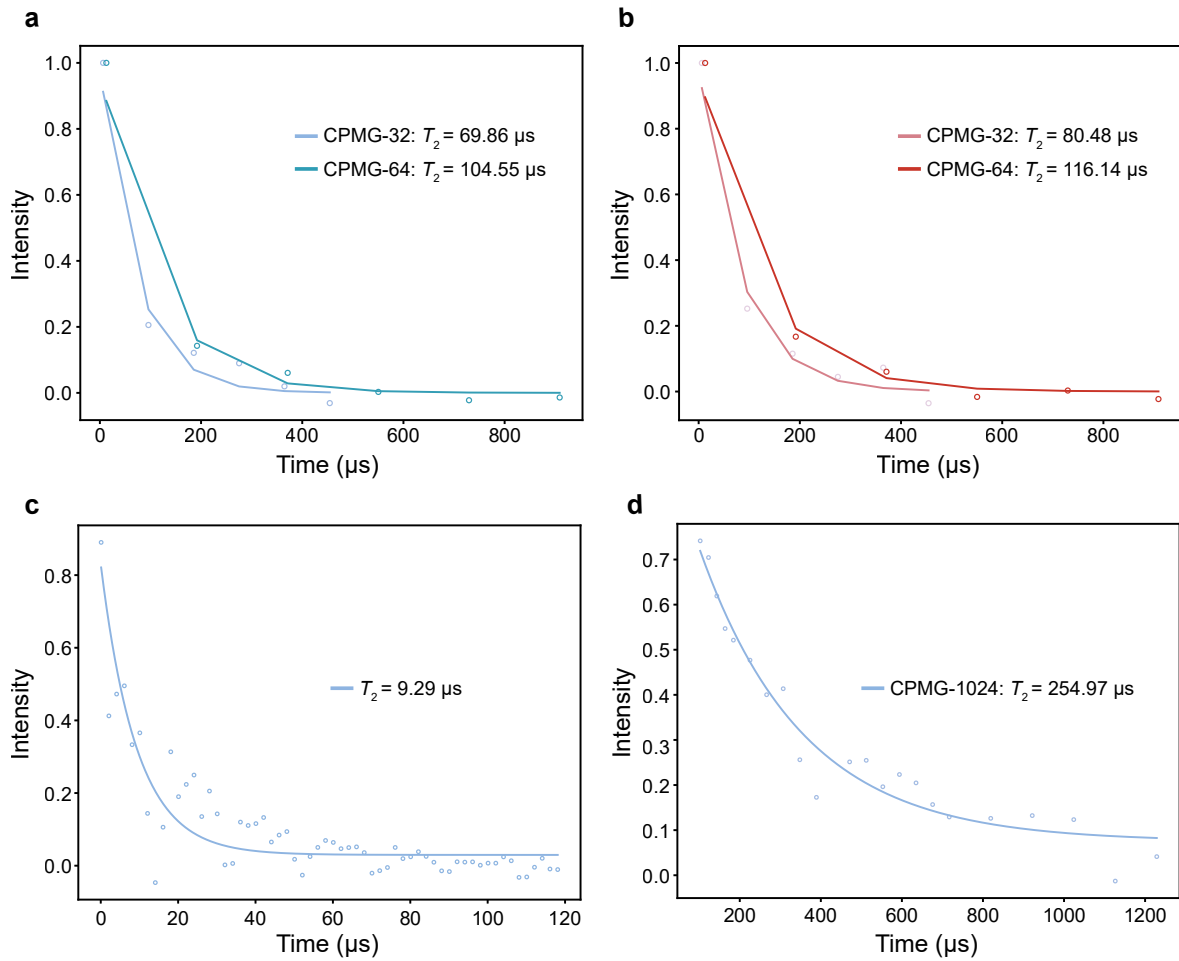


Figure S5. Optically detected magnetic resonance spectroscopic characterization results of diamond NV Centers. **a,b**, signal decay curves of CPMG-32 and CPMG-64 with HPC and TPC, respectively. **c**, Hahn echo decay curve. **d**, echo decay curve collected by CPMG-1024 with TPC.

5.3 Effective state fidelity test

5.3.1 Quantum state tomography

As previously mentioned (see equation (40)), $s_{x,y,z}^i$ are required for state reconstruction. To obtain these values, $\frac{\pi_{x,-y}}{2}$ pulses were applied before measurements for $s_{y,x}^i$. No extra pulse was needed to measure s_z^i .

5.3.2 Test on the trapped ion qubit

The tests involve CP- m and UDD- m . CP- m can be represented as $(\pi_x/2 - (\tau - \pi_x - \tau)_m - echo)$. For CP- m experiments, the τ value was fixed to be 50 μ s. For the UDD- m sequences, the t value was fixed to be 1200 μ s. TPC's results were obtained from an average of 2048 shots for each phase cycling step; HPC's results were obtained from an average of 256 shots for each phase cycling step.

5.3.3 Test on the superconducting qubit

For CP- m experiments, the τ value was fixed to be 250 ns. For the UDD- m sequences, the t value was fixed to be 100 μ s. HPC results were obtained from an average of 1024 shots for each phase cycling step. TPC results were obtained similarly. Considering that TPC involves only two phase cycling steps, we intentionally added redundant experiments to align with HPC's number of shots.

5.3.4 Results of the superconducting qubit

Regarding UDD- m , HPC preserves F^{eff} above 99.3% up to 16 inversion pulses, whereas TPC gives rise to significantly smaller values, with F^{eff} dropping to 97.3% for UDD-16 and 53.5% for UDD-64. We further deliberately introduced systematic error to each pulse. For CP- m with $\pi/28$ systematic error, HPC retains F^{eff} above 99.3% for $m = 2-128$, whereas TPC causes an oscillation of F^{eff} , which drops to 0 for m being 32 and 96. Therefore, HPC maintains remarkable robustness even under relatively large systematic error.

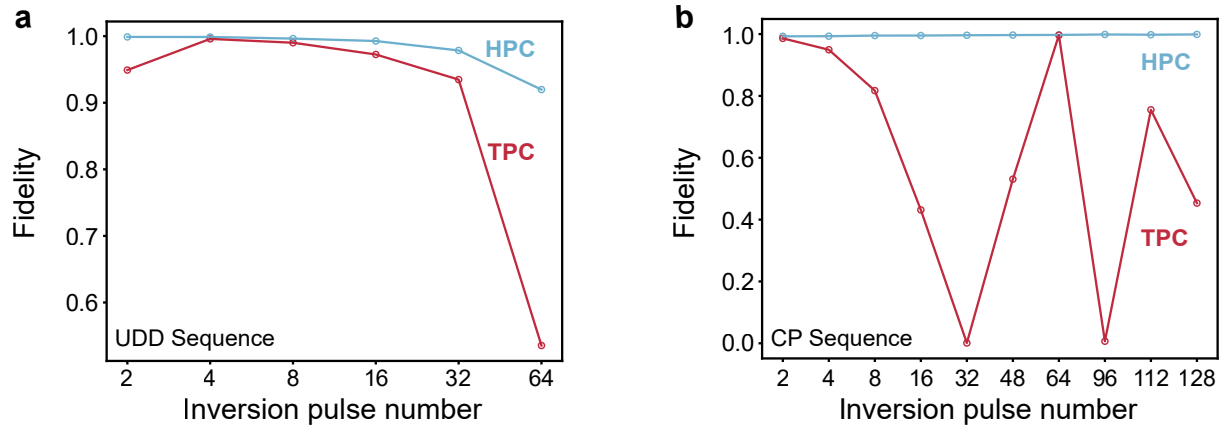


Figure S6. Effective state-fidelity tests on single superconducting transmon qubit. **a**, results for UDD experiments with TPC and HPC. **b**, results for CP experiments with TPC and HPC. A $\pi/28$ systematic error was introduced to each inversion pulse.

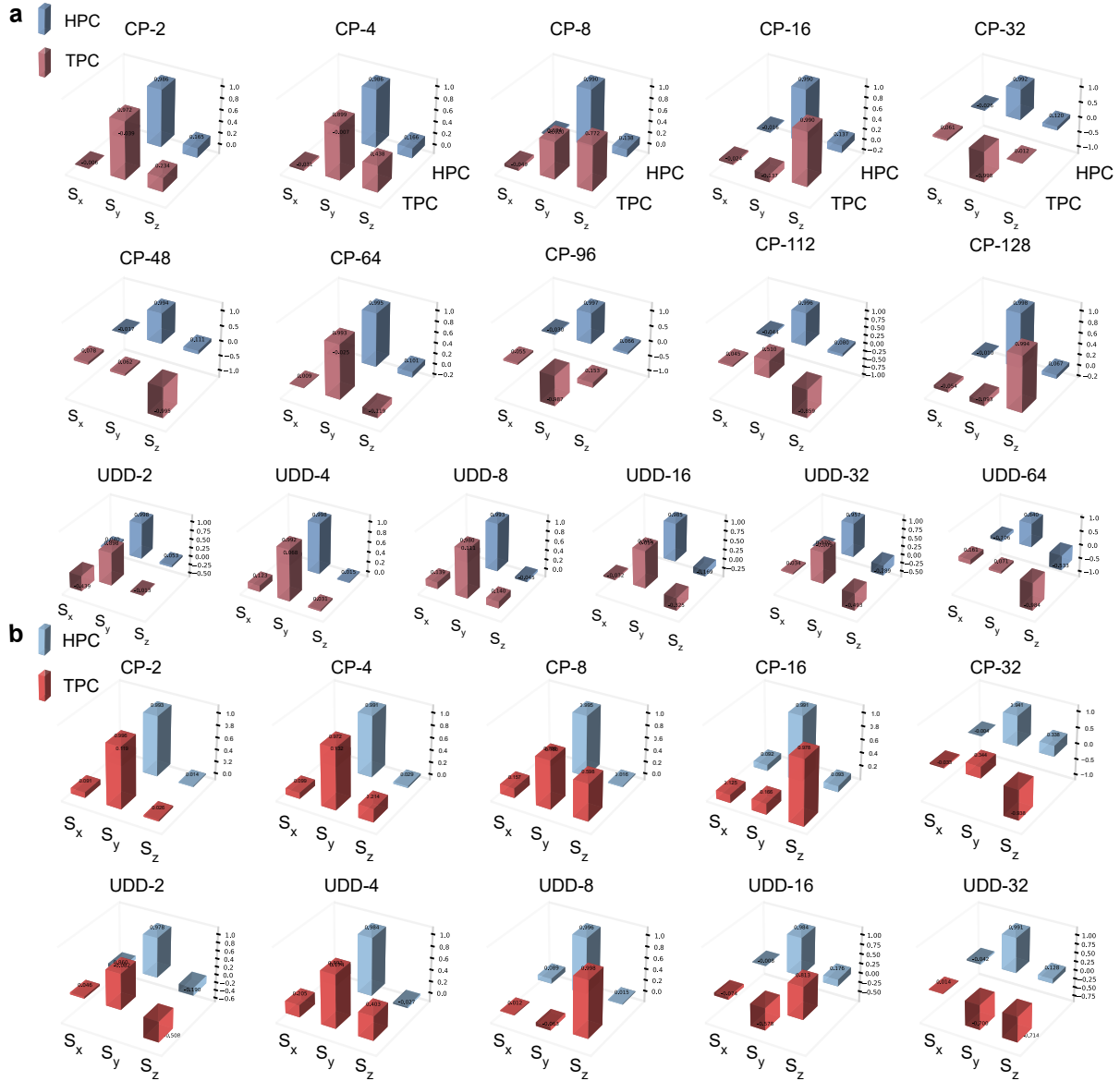


Figure S7. Quantum state tomography results of **a**, single superconducting transmon qubit and **b**, single trapped ion qubit.

Table 5: T_2 of $(\text{PPh}_4)_2[\text{Cu}(\text{mnt})_2]$ under IDD- m

m	Phase cycling	T_2 (μs)	IDD
8	HPC	14.85	CPMG
8	TPC	16.80	CPMG
14	HPC	17.17	CPMG
14	TPC	18.50	CPMG
16	HPC	17.39	CPMG
16	TPC	20.58	CPMG
30	HPC	18.80	CPMG
30	TPC	24.63	CPMG
64	HPC	21.13	CPMG
64	TPC	33.13	CPMG
128	HPC	24.42	CPMG
128	TPC	43.53	CPMG
256	TPC	64.05	CPMG
512	TPC	98.91	CPMG
4	HPC	13.70	UDD
6	HPC	16.88	UDD
8	HPC	23.22	UDD
10	HPC	30.56	UDD
12	HPC	31.56	UDD
14	HPC	35.72	UDD

Table 6: T_2 of COF-5 under IDD- m

m	Phase cycling	T_2 (μs)	IDD
2	CPC	5.88	CPMG
4	CPC	7.57	CPMG
6	HPC	9.63	CPMG
8	HPC	11.06	CPMG
16	HPC	14.47	CPMG
32	HPC	19.91	CPMG
2	TPC	6.16	CPMG
4	TPC	8.79	CPMG
8	TPC	12.36	CPMG
16	TPC	17.03	CPMG
32	TPC	25.48	CPMG
64	TPC	33.74	CPMG
128	TPC	43.23	CPMG
256	TPC	56.70	CPMG